



TECHNISCHE
UNIVERSITÄT
WIEN



Vienna University of Technology

Diploma Thesis

Influence of stress ratio on the torsional fatigue behaviour of 17-4PH stainless steel used for biomedical applications

carried out for the purpose of obtaining the degree of Master of Science (MSc or Dipl.-Ing. or DI), submitted at TU Wien, Faculty of Mechanical and Industrial Engineering, by

Seyedmasoud Chehrehrazi

Mat.Nr.: 1529377

under the supervision of

Univ.Prof. Mag. Dr.rer.nat. Helga Lichtenegger

Dipl.-Ing. Dr.techn. Bernd Schönbauer

Institute of Physics and Materials Science

University of natural resources and life sciences

Signature

Affidavit

I declare in Lieu of oath, that I wrote this thesis and performed the associated research myself. Using only literature cited in this volume. If text passages from sources are use literally, they are marked as such.

I confirm that this work is original and has not been submitted elsewhere for any examination, nor is it currently under consideration for a thesis elsewhere.

Signature: _____

Date: _____

Acknowledgments

I would like to express my gratitude to Prof. Helga Lichtenegger for giving me the opportunity to work on this project in Institute of Physics and Materials Science at BOKU university. Furthermore, I would like to sincerely thank my supervisor, Dr. Bernd Schönbauer for his continuous support and useful comment through my thesis research. Undoubtedly, this work would not be successfully finished without his valuable guidance.

Last but not least, I would like to appreciate my family; my parents and also my wife for their support during this work.

Abstract

Precipitation-hardened chromium-nickel-copper stainless steel 17-4PH has a high strength, toughness and good corrosion resistance. According to these features, the 17-4PH stainless steel has a great application in biomedical advices such as hand tools and surgical staplers. In this study, the fatigue behavior of 17-4PH stainless steel under torsional loading condition in the very high cyclic fatigue regime was studied. To test the specimens in reasonable time, the ultrasonic fatigue testing equipment was used, which applies a sinusoidal load at a frequency of about 20 kHz. The results were compared with torsional tests that were conducted using conventional servohydraulic testing. Furthermore, the frequency effect and also the effect of delta ferrite grains on initiation of cracks at different loading frequencies are discussed. In addition, the \sqrt{area} as a geometric parameter is used to determine the effect of small artificial defects on the torsional fatigue limit. Furthermore, the effect of different R -ratios on smooth and defect containing specimens is investigated.

Contents

| | |
|---|----|
| Declaration | |
| Acknowledgment | |
| Abstract | |
| 1 Introduction..... | 1 |
| 1-1 Motivation | 1 |
| 1-2 Related work and scope of the present work | 5 |
| 2 Theoretical background..... | 7 |
| 2-1 Fatigue in materials | 7 |
| 2-1-1 Description of cyclic loading | 8 |
| 2-1-2 Stress versus life ($S - N$) curves | 9 |
| 2-1-3 Different phases of fatigue life..... | 11 |
| 2-1-4 Stress concentration and fatigue notch effect..... | 13 |
| 2-1-5 Stress intensity factor | 14 |
| 2-1-6 Fatigue crack propagation for long crack | 16 |
| 2-1-7 Short cracks propagation | 18 |
| 2-1-8 Threshold conditions for small cracks, Kitagawa-Takahashi diagram | 19 |
| 2-1-9 \sqrt{area} parameter mode I..... | 20 |
| 2-2 Stainless steel | 24 |
| 3 Materials and test procedure | 26 |
| 3-1 Testing material..... | 26 |
| 3-2 Specimen shape and preparation | 28 |
| 3-3 Ultrasonic fatigue testing equipment..... | 32 |
| 4 Results and discussion..... | 34 |
| 4-1 Smooth specimens with $R = -1$ | 34 |
| 4-1-1 Influence of specimen shape..... | 36 |
| 4-1-2 Influence of loading direction..... | 37 |
| 4-2 Influence of frequency..... | 39 |
| 4-3 Influences of small defects | 53 |
| 4-4 Influence of stress ratio..... | 57 |
| 5 Conclusions | 63 |
| Bibliography..... | 65 |

Chapter 1

Introduction

1-1 Motivation

Biomaterials science, or the study of the application of materials science in biology and medicine, originated in the early 1930's following the first industrial production of synthetic plastics [1]. Their ease of fabrication led to many experiments in human implants, in particular. Most early implants failed due to the limited understanding of biomaterials toxicology at the time, however. Among the wide range of materials that have been developed for biomaterials applications (examples are given in Table 1.1), the metal base materials play a major role, especially in implants and medical instruments.

Table 1. 1: Examples of some biomaterials and their applications (according to [1])

| Applications | Type of materials |
|-----------------------------------|--|
| Skeletal system | |
| Joint replacements (hip, knee) | Titanium, Ti-Al-V alloy, stainless steel, polyethylene |
| Bone plate for fracture fixation | Stainless steel, cobalt-chromium alloy |
| Bone cement | Poly methyl methacrylate |
| Bony defect repair | Hydroxyl apatite |
| Artificial tendon and ligament | Teflon, Dacron |
| Dental implant for tooth fixation | Titanium, alumina, calcium phosphate |
| Cardiovascular system | |
| Blood vessel prosthesis | Dacron, Teflon, polyurethane |
| Heart valve | Reprocessed tissue, stainless steel, carbon |
| Catheter | Silicone rubber, Teflon, polyurethane |
| Organs | |
| Artificial heart | Polyurethane |
| Skin repair template | Silicone-collagen composite |
| Heart-lung machine | Silicone rubber |
| Senses | |
| Cochlear replacement | Platinum electrode |
| Intraocular lens | Poly methyl methacrylate, silicone rubber, hydrogel |
| Contact lens | Silicone-acrylate, hydrogel |
| Corneal bandage | Collagen, hydrogel |
| Medical devices | |
| Surgical scissors | Stainless steel |
| Scalpels | Stainless steel |
| Surgical suture | Nylon, polyester, Polyglycolide |

The Properties such as high strength, corrosion resistance, formability, etc., along with the natural availability of these metals, has led to their selection for metallic implants and medical instrument (examples are shown in Fig. 1.1).

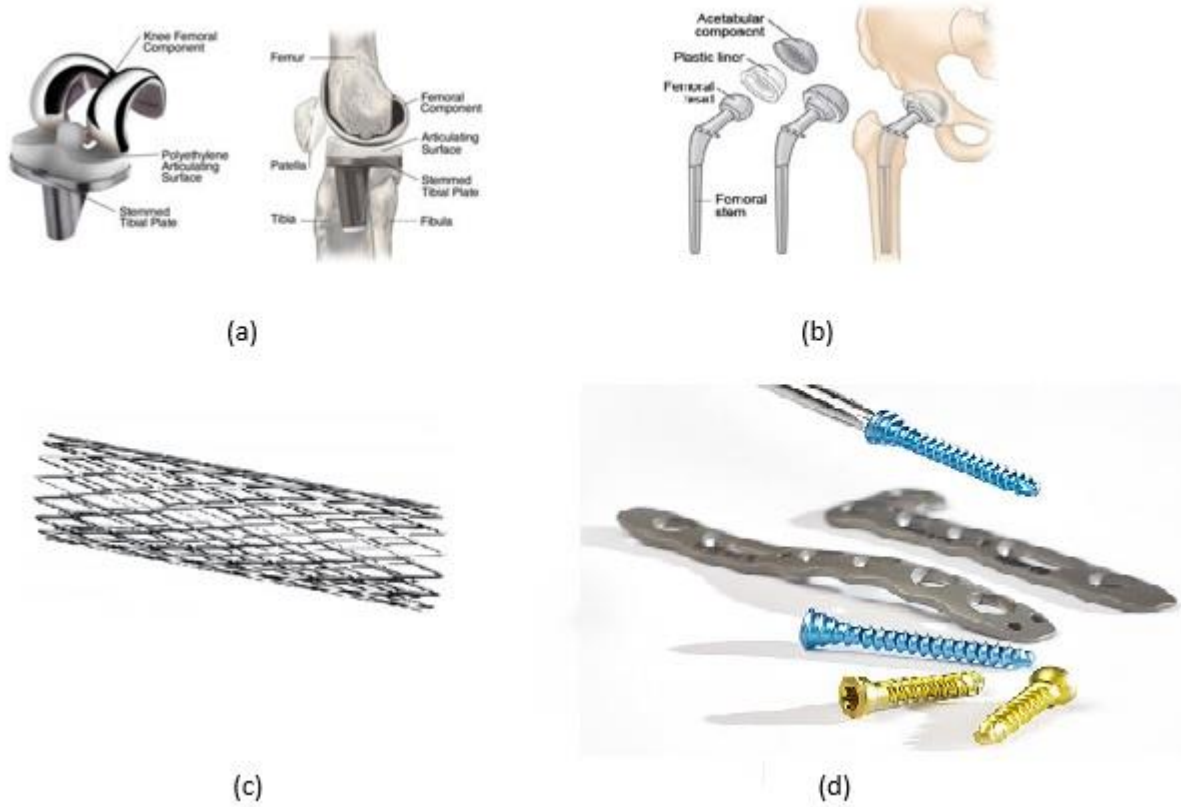


Fig. 1. 1: Examples of metallic implant: (a) artificial knee [2], (b) artificial hip joint [3], (c) artery stent [4], (d) Orthopedic Implant Plates and Screw [5].

The type of metal used in biomedical applications depends on the needs of specific implant applications. 316L type stainless steel (316L SS) is the most commonly used alloy in implants ranging from cardiovascular to otorhinolaryngological applications [6]. However, when an implant requires high wear resistance such as for artificial joints, CoCrMo alloys are often chosen instead [7]. Table 1.2 summarizes the types of metals generally used for different categories of implants.

Table 1. 2: Implants division and type of metals used (according to [8])

| Division | Example of implants | Type of metal |
|----------------|--|---|
| Cardiovascular | Stent Artificial valve | 316L SS; CoCrMo; Ti Ti6Al4V |
| Orthopedic | Bone fixation (plate, screw, pin) Artificial joints | 316L SS; Ti; Ti6Al4V CoCrMo; Ti6Al4V; Ti6Al7Nb |
| Dentistry | Orthodontic wire Filling | 316L SS; CoCrMo; TiNi; TiMo AgSn(Cu) amalgam, Au |
| Craniofacial | Plate and screw | 316L SS; CoCrMo; Ti; Ti6Al4V |
| Otorhinology | Artificial eardrum | 316L SS |

In order to select the most proper metal alloy for different implants, the application of implant should be considered. For example, stents should have adequate plasticity for expansion and rigidity to maintain dilatation [9]. For orthopedic implants, metals must have excellent toughness, elasticity, rigidity, strength and resistance to fracture. For total joint replacement, metals must be wear resistant [6] so debris formation from friction can be avoided. It should also be noted that both static and dynamic mechanical loads are generated in many implants. Although static strength criteria such as stiffness are well characterized for most implant materials, dynamic criteria such as fatigue strength are not as well understood. In addition to mechanical properties, metallic implants must also have an adequate resistance to the highly corrosive environments in the human body.

Like in other fields of science and technology, steel alloys are constantly being optimized and improved. New materials in the biomedical field, especially when used as implants, must pass various tests including as mechanical testing, biocompatibility testing, and so on before they may be used. The aim of this study is to introduce and perform torsional fatigue testing on 17-4PH stainless steel, which has among the highest levels of corrosion resistance of all metallic biomaterials and has growing applications in devices such as hand tools and surgical staplers. Previous studies have revealed that 17-4PH stainless steel shows adequate biocompatibility (e.g. [10],[11]), and although there are many publications documenting the static mechanical properties of this material (e.g. [12],[13]), the fatigue properties of 17-4PH stainless steel in the regime of very long lifetimes have not been as thoroughly investigated. One reason for this lack of research is the significant time investment typically required for fatigue testing. Recent improvements in

ultrasonic fatigue testing allow for faster characterization of the fatigue behavior experienced under high cyclic loading conditions in biomedical devices, however. Tests with more than one billion cycles can be completed within several days, whereas conventional cyclical fatigue testing equipment requires months or even years. A new experimental test setup that applies cyclic torsion loads at ultrasonic cycling frequencies in combination with superimpose static shear loads has been developed at the Institute of Physics and Materials Science of the University of Natural Resources and Life Sciences, Vienna (BOKU) [14]. This method enables to perform high-frequency torsion fatigue test with different stress ratios (i.e., ratios of minimum and maximum stress). In this study, we have conducted the torsional fatigue test of 17-4PH stainless steel with this ultrasonic fatigue test equipment at a frequency of 20 kHz. Fully reversed loading as well as superimposed static shear loads were applied. Additionally, different artificial holes were drilled in some specimens in order to investigate the defect tolerance systematically.

1-2 Related work and scope of the present work

The main purpose of this research is to investigate the fatigue behavior of 17-4PH stainless steel under torsional loading condition in the long-lifetime regime. To fatigue the specimens, the ultrasonic fatigue testing equipment was used, which applies a sinusoidal load at a frequency of about 20 kHz. Schönbauer et al. have performed comprehensive fatigue tests on 17-4PH stainless steel using the ultrasonic equipment but under tension-compression loading (e.g.[15],[16]). Furthermore, the stress ratio dependency under uniaxial loading was investigated. In the present work, the results obtained from very high cycle fatigue tests under torsional loading are compared with those from tension-compression tests. Furthermore, the effect of load ratio, R , under torsion loading condition is investigated.

Already in a previous study, the fatigue life of 17-4PH stainless steel has been investigated at a test frequency of about 20 Hz via conventional servo hydraulic fatigue test equipment [17]. To determine the frequency effect, in this research, we have compared the recent results obtained with ultrasonic fatigue testing with the low-frequency test results. In this regards, the effects of delta ferrite grains on the fatigue strength depending on the loading frequency has been investigated. The form of delta ferrite grain and also non-propagation cracks inside the specimen was obtained by grinding a specimen's surface in steps.

Murakami and Endo introduced another approach to estimate the fatigue strength of material, as well. This model, known as \sqrt{area} parameter model (square root area parameter model), can predict the fatigue limit using only two parameters: the square root of the projected area of a small defect or a crack perpendicular to the loading direction, \sqrt{area} , and the Vickers hardness of material, HV , [18]. We have estimated the fatigue limit of 17-4PH stainless steel under torsional loading conditions using this model.

Chapter 2

Theoretical background

2-1 Fatigue in materials

Components of machines, vehicles, and structures are frequently subjected to repeated loads, and the cyclic applied stresses can lead to microscopic physical damage to the materials involved. Even at stresses well below a given material's ultimate strength, microscopic damage caused by cyclic loading can add up until it develops into a crack or other macroscopic damage that leads to the failure of a component. This process of damage and failure due to cyclic loading is called fatigue.

Fatigue failure in metallic materials is a well-studied phenomenon. Scientific investigation of fatigue dates to the 18th century when the first fatigue test results were published by Wilhelm Albert [19]. During the 19th century the causes of fatigue failure were poorly understood, however, because fatigue damage could not be easily seen and failure appeared to occur spontaneously. Nowadays, it is well known that cyclic loading even significantly below critical static stresses can lead to nucleation and the initiation of small cracks, which can be followed by crack propagation and eventually complete failure.

To better understand the mechanism of fatigue, some definitions are provided below.

2-1-1 Description of cyclic loading

In many practical applications, as well as in fatigue testing procedures, the maximum and minimum cyclic stress levels, σ_{\max} and σ_{\min} , are constant. An example diagram of a constant amplitude stress versus time plot is illustrated in Fig. 2.1 and Fig. 2.2. It is noted that cyclic loading can also be applied with variable amplitude too. The difference between maximum and minimum value of stress, $\sigma_{\max} - \sigma_{\min}$, is known as the stress range, $\Delta\sigma$. Half of the stress range is called the stress amplitude, σ_a . Furthermore, the average of maximum and minimum value called the mean stress, σ_m . The cyclic loading is called fully reversed cycling if the value of mean stress is zero (see Fig. 2.1), though in many practical cases of pre-loading, the mean stress is not zero. (see Fig. 2.2)

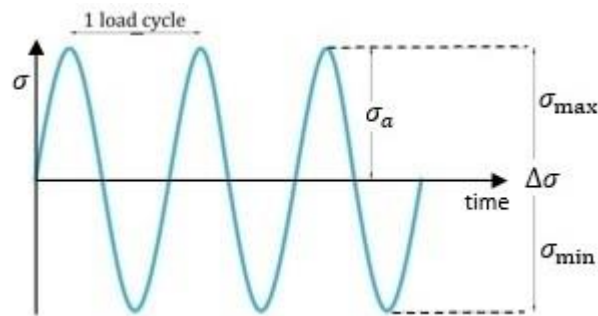


Fig. 2. 1: Constant amplitude cycle loading with $\sigma_m = 0$, (fully reversed cycling loading).

Mathematical expressions for these parameters are:

$$\Delta\sigma = \sigma_{\max} - \sigma_{\min}, \quad \sigma_m = \frac{\sigma_{\max} + \sigma_{\min}}{2} \quad (2-1)$$

The ratio of σ_{\max} and σ_{\min} , R , is defined as the stress ratio:

$$R = \frac{\sigma_{\min}}{\sigma_{\max}} \quad (2-2)$$

For fully reversed cycling loading, $R = -1$.

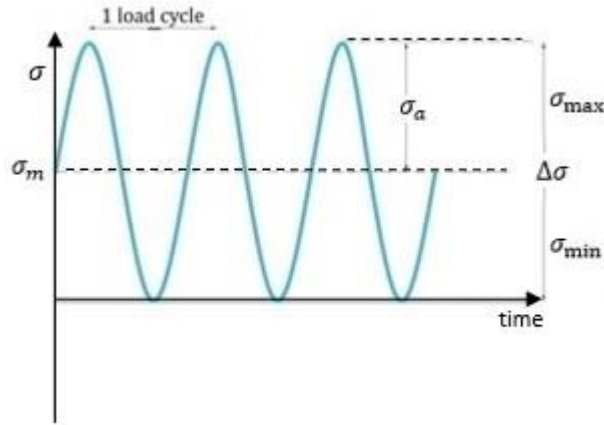


Fig. 2. 2: Constant amplitude cycle loading with positive mean stress σ_m .

2-1-2 Stress versus life ($S - N$) curves

If a component is cyclically loaded with critical stress amplitude with the maximum stress below the tensile strength, failure will occur after a specific number of cycles, N . If the test is repeated at a higher stress amplitude, the number of cycles until failure will be smaller. The result of different stress amplitudes versus the number of cycles until failure can be plotted in a diagram to obtain a stress-life curve, also called an $S-N$ curve. Wöhler for the first time carried out experiments to obtain $S-N$ curves in the 19th century [19]. Therefore, $S-N$ curves are also called Wöhler curves.

Fig. 2.3 shows the typical $S-N$ curve schematically. When performing $S-N$ tests, the samples are tested at different stress amplitude levels. A Wöhler curve is used to illustrate the results by showing logarithmic plots of the stress range $\Delta\sigma$ (or the stress amplitude σ_a) over the number of load cycles. The curve can be divided into three regions:

- Low cycle fatigue (LCF) refers to the range at which the applied maximum stresses exceed the yield strength of material, but is below the tensile strength. In this case, high plastic deformations take place. The number of cycle to failure is up to $10^4 - 10^5$. If the applied maximum stress is above the tensile strength of the material, R_m , the failure occurs within one load cycle.

- High cycle fatigue (HCF) refers to the range at which the maximum cyclic stresses apply below the yield strength of material. The material in this case needs high number of loading cycles up to 10^7 before the failure occurs. The range of the $S-N$ curve can be approximated by a straight line in double logarithmic representation is described by the Basquin's equation:

$$\Delta\sigma^k \cdot N = \text{Constant} \quad (2-3)$$

The exponent k denotes the slope of the time-stability line and is dependent on the material.

- In some materials, if the amplitude of applied stress is below a specific value, the Wöhler line runs horizontally, which means that no fatigue failure occurs at this stress level. The fatigue limit refers to this stress amplitude. If a specimen is subjected to cyclic loading below the fatigue limit, the specimen would survive at unlimited number of loading cycles.
- There are some components which should last huge number of cycle loading. Very high cycle fatigue (VHCF) refers to fatigue life more than 10^8 cycles. At the present time, it is well known that in some materials, the fatigue failure can occur with maximum applied cyclic stresses even below the fatigue strength of material. It means that for some materials, the fatigue strength cannot be defined and failure can occur even after very high number of cycles too.

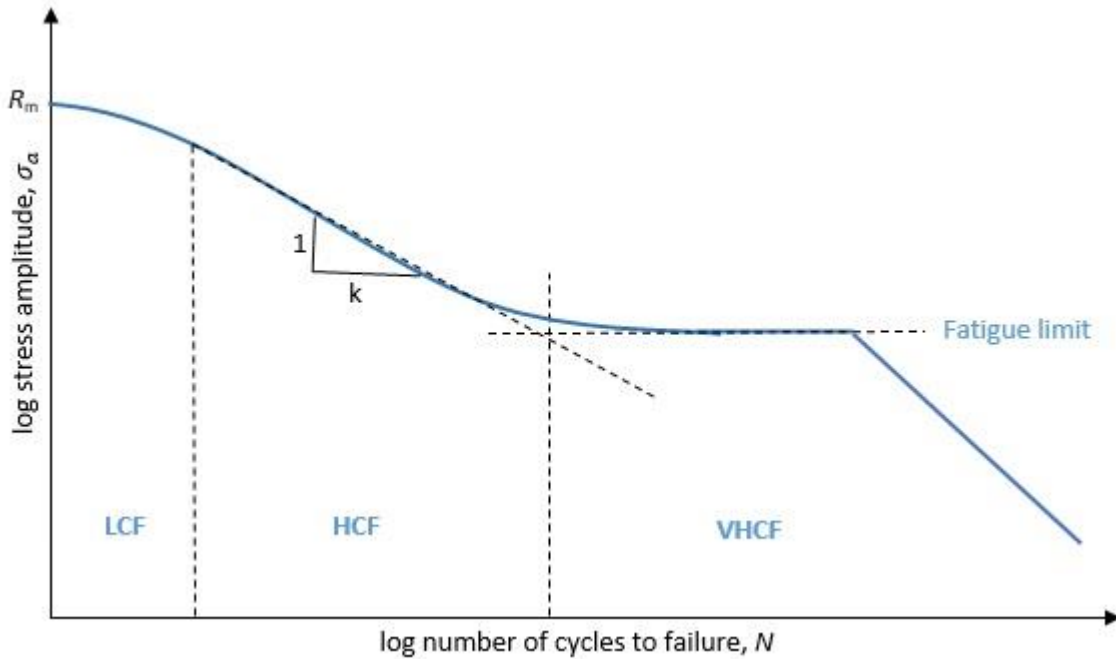


Fig. 2. 3: Typical S-N curve.

2-1-3 Different phases of fatigue life

As shown in Fig. 2.4, the fatigue life of material can be divided in two major mechanisms before final failure, nucleation of micro cracks (initiation period) and propagation of micro cracks to macro cracks (crack growth period). Generally, the micro cracks initiate from slip bands and can occur immediately if the maximum value of applied cyclic stress reaches the fatigue limit of material. The micro cracks can remain invisible in micro grains boundary for considerable period of total fatigue life due to microstructure effects [20]. However, after a while, the micro cracks can be extended beyond the grain boundaries. In this period of fatigue life, the crack growth rate is increased until the final failure occurs.

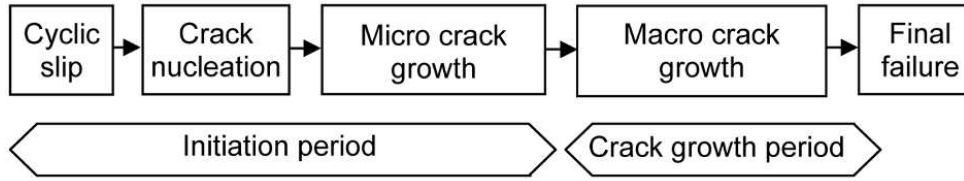


Fig. 2. 4: Different period of the fatigue life [20].

A schematic of the typical fatigue fracture surface is shown in Fig. 2.5. As mentioned earlier, cracks initiate at slip bands or stress concentrations, and the fatigue fracture surface is perpendicular to an applied stress. Generally, the fatigue fracture surface consists of two distinct regions: a smooth portion which corresponds to the beginning stages of fatigue life when the cracks grow slowly, and a rough and granular portion which corresponds to the last stage when the remaining material cannot support the applied stress and the crack grows rapidly until failure.

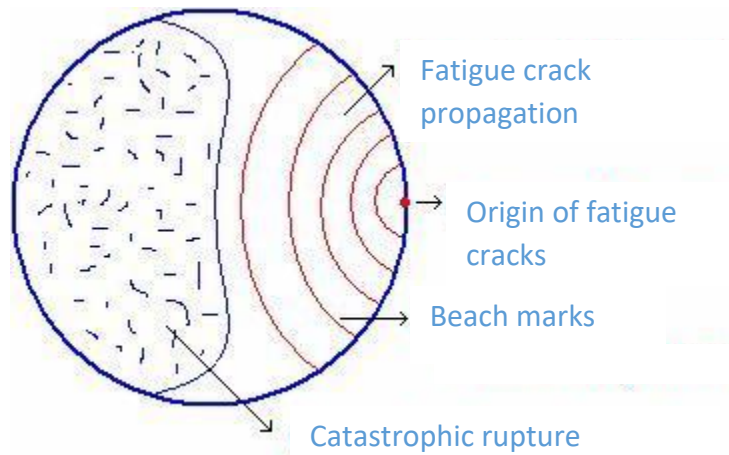


Fig. 2. 5: Schematic fatigue fracture surface.

Additional characteristic patterns on the surface of fatigue fractures are called beach marks and striations. Both of these circular patterns indicate the position of the crack tip, and appear as concentric rings that expand away from the crack initiation site. Beach marks are macroscopic rings and can be observed without the assistance of a microscope, while striations are microscopic features that must be seen with electron microscopy. The beach mark is correspondent with changes in crack growth rates and is related to a package of cyclic loading. However, the origin

of striation is the plastic zone which is produced in front of the crack tip after any single cycle loading. In Fig. 2.6, an example of striations under a Scanning Electron Microscope (SEM) is illustrated.

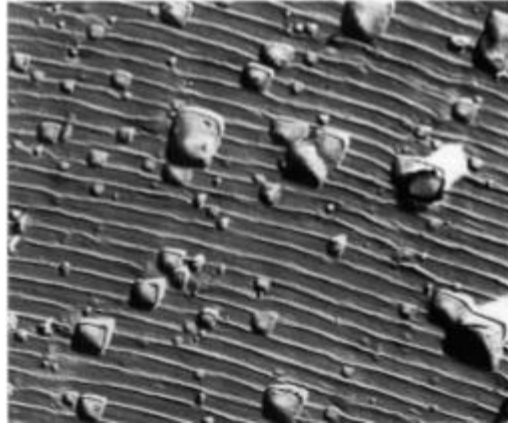


Fig. 2. 6: Typical form of fatigue striation under SEM [21].

2-1-4 Stress concentration and fatigue notch effect

The stress near a hole or at a notch root has a higher value than stresses at the other locations in a structure. This phenomenon is called stress concentration. The stress concentration factor, K_t , is the ratio between the peak stress near the notch and the nominal stress in the area surrounding the notch. Stress concentration values for various notches shape have been collected in standard handbooks (e.g., [22]). As an example, Fig. 2.7 shows an elliptical hole in a wide plate under uniaxial tension in the y-direction. The stress concentration factor, K_t , in this case is [23]:

$$K_t = 1 + \frac{2a}{b} \quad (2-4)$$

According to Eq. 2-4, as the elliptical hole becomes closer to a circular hole, the stress concentration factor tends towards 3.

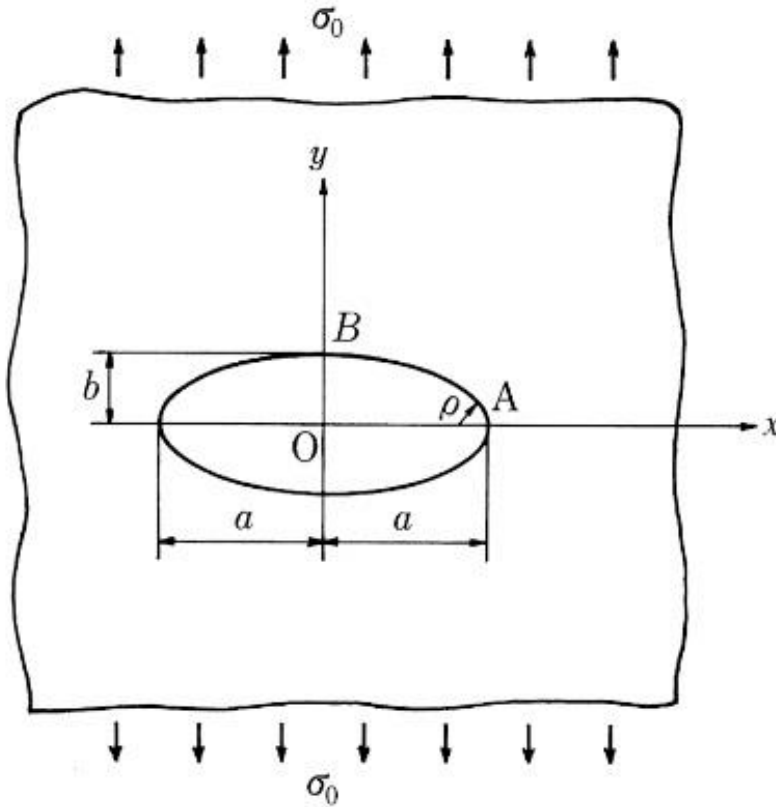


Fig. 2. 7: Stress concentration at an elliptical hole: $\sigma_{yA} = \left(1 + \frac{2a}{b}\right)\sigma_0$, $\sigma_{xB} = -\sigma_0$ [23].

Fatigue failure is often initiated from holes or notches where the local stress is higher due to stress concentrations. To avoid unexpected fatigue failure, the effect of stress concentrations should be well understood.

2-1-5 Stress intensity factor

In the case of Fig. 2.7, we can define the crack as a slender ellipse with a root radius, ρ , of almost zero. According to Eq. 2-4, the stress concentration caused by an extremely slender elliptical hole, i.e. at the crack tip, becomes infinite regardless of the length of the crack. Therefore, it is not appropriate to use the definition of stress concentration factor at the tips of cracks. Irwin has presented a new parameter known as stress intensity factor, SIF, which is defined as 'the parameter describing the intensity of the singular stress field in the vicinity of a crack tip' [24]. Fig. 2.8 shows a crack of length $2a$ in the x direction in a wide plate under a uniaxial tensile stress, σ_0 , in the y -direction.

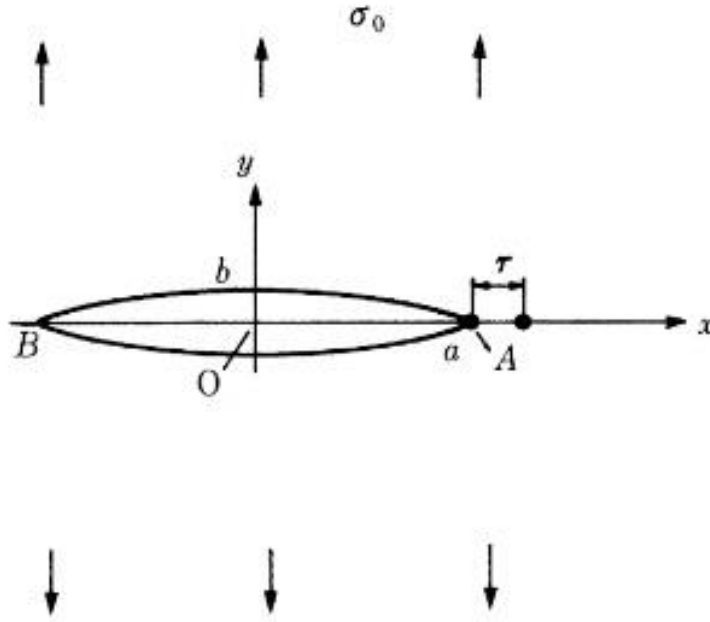


Fig. 2. 8: Two dimensional crack of length $2a$ [23].

From the perspective of fracture mechanics, three modes of fracture are defined, which are illustrated in Fig. 2.9. These basic fracture modes are usually called Mode I (opening mode), Mode II (sliding mode), and Mode III (tearing mode). It should be noted that we can characterize every crack by one of these modes or some combination of the three.

For mode I, or opening mode, where the crack surfaces move in opposite direction, the stress intensity factor is written as [23]:

$$K_I = \sigma_0 \sqrt{\pi a} \quad (2-5)$$

In which, the stress intensity factor for mode I, K_I , is in $\text{MPa}\sqrt{\text{m}}$ and the uniaxial remote tensile stress, σ_0 , is in MPa.

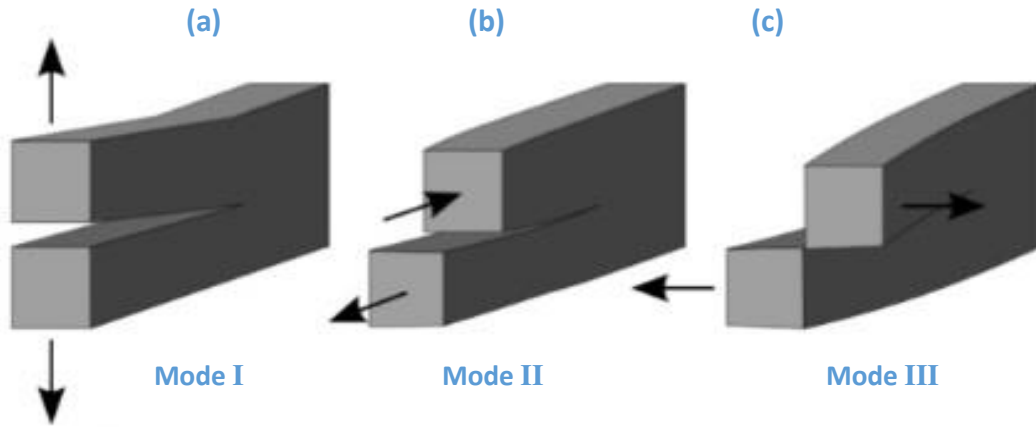


Fig. 2. 9: Modes of failure, (a): Mode I (opening mode), (b): Mode II (sliding mode), (c): Mode III (tearing mode) [25]

2-1-6 Fatigue crack propagation for long crack

Considering the low portion of plastic deformation in front of the crack tip, the crack growth can be characterized by linear elastic fracture mechanics (LEFM) [25]. In point of linear elastic fracture mechanics, it is assumed that all structures have already some micro cracks before any loading with an initial length size, a_0 after applying a cyclic loading, these micro cracks should be extended to a critical size, a_c , when the failure takes place [26] (see Fig. 2.10).

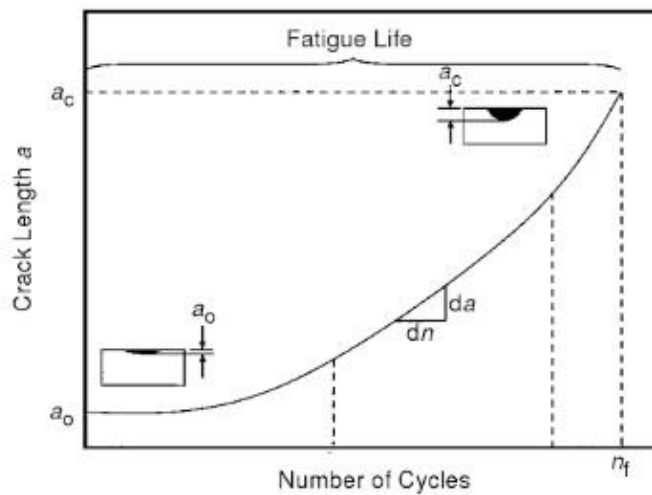


Fig. 2. 10: Crack length as a function of cycle [27].

In the fracture mechanics approach, the rate of crack growth per loading cycle, da/dN , is plotted as the function of stress intensity factor, K . There is a correlation between the macro crack growth rate and the stress intensity factor [20]. An idealized da/dN versus ΔK curve is shown in Fig. 2.11.

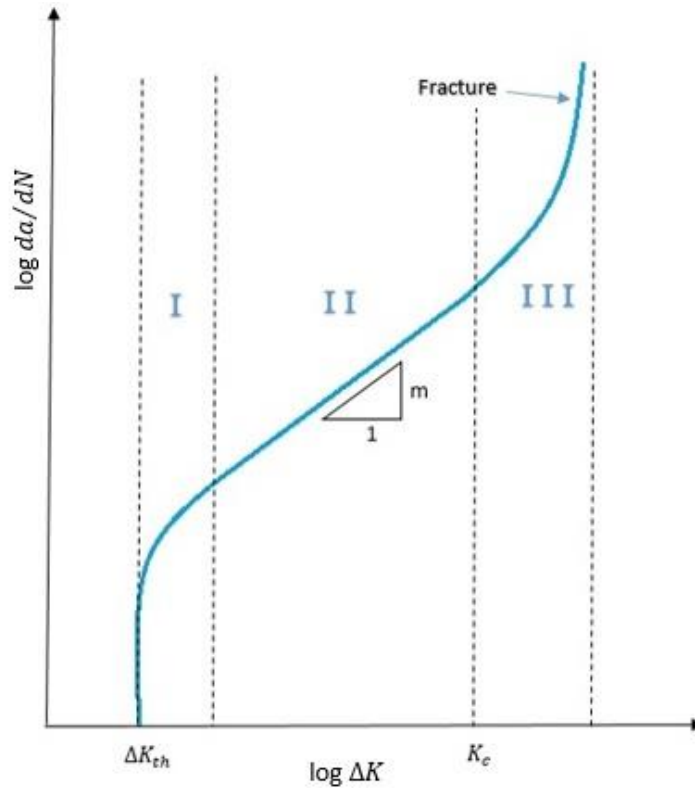


Fig. 2. 11: Typical fatigue-crack-growth diagram showing three different regimes.

There are three regions in this diagram. In region I, ΔK_{th} is the fatigue crack growth threshold, below which there is not any crack propagation. So, the crack growth rates approach zero. In region II, the crack growth rate is linear and can be determined by power law equations, such as the Paris equation as follow [27]:

$$\frac{da}{dN} = C(\Delta K)^m \tag{2-6}$$

where a is the crack size, N is the number of cycles, C and m are constant parameters related to material, geometry, load, and fatigue stress conditions which is determined by experimentation, and

$\Delta K = K_{max} - K_{min}$ is the stress-intensity factor range corresponding to the alternating stress and can be expressed in terms of $\Delta\sigma$:

$$\Delta K = \Delta \sigma \cdot \sqrt{\pi \cdot a} \cdot Y \quad (2-7)$$

Where $\Delta \sigma$ is the nominal stress range, a is the crack length and Y is a geometry factor, which is related to sample dimension, the crack geometry, and the type of stress.

In the region III, the crack growth rate increases rapidly and when a critical value of the stress intensity factor (related to the maximum stress, σ_{\max}) reaches $K_{\max} = K_{IC}$, complete failure results.

2-1-7 Short cracks propagation

Crack propagation behavior of short (or small) cracks differs from long cracks. According to Suresh et al. the short cracks can be classified as below [28]:

- 1- Microstructurally small cracks which is referred to crack sizes comparable to the size of microstructural dimension such as grain size.
- 2- Mechanically small cracks which is comparable to the plasticity zone which is formed in front of the crack's tip.
- 3- Physically small cracks with length smaller than one or two millimeter.

Pearson has reported that the short cracks significantly grow up faster than longer cracks subjected to the same applied stress [29]. The schematically relation of fatigue cracks growth rate as a function of the stress intensity factor range for short cracks (dashed lines) in comparison with long cracks is illustrated in Fig. 2.12. It can be seen that for the cracks smaller than a specific length, the crack growth rate may decrease with increasing the crack length. This is due to the built up of a plastic wake which caused so-called plasticity-induced crack closure. It should be noted that short cracks can propagate also for applied stress intensity factor ranges below the threshold ΔK_{th} for long cracks. Ignoring the short cracks propagation behavior can lead to overestimate of fatigue strength.

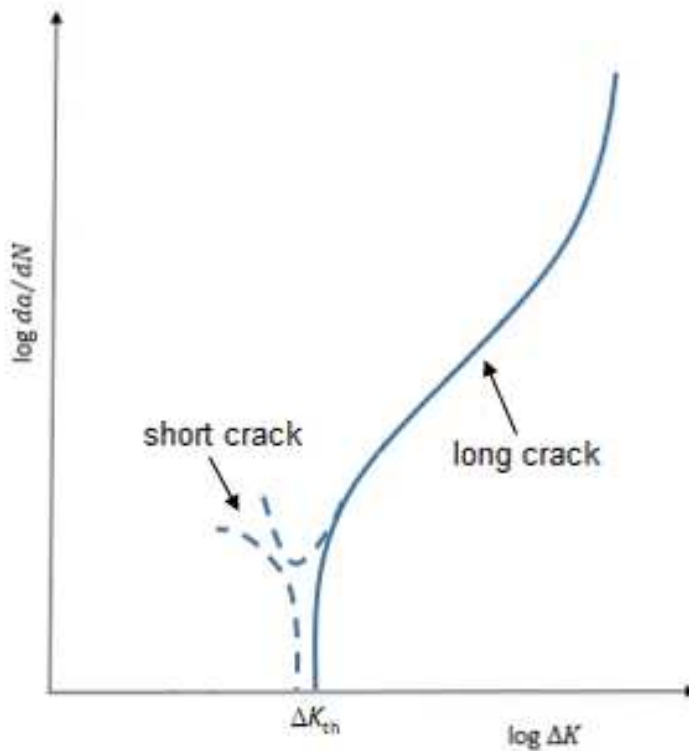


Fig. 2. 12: Schematic crack growth rate behavior of short and long cracks.

2-1-8 Threshold conditions for small cracks, Kitagawa-Takahashi diagram

One of the most important approaches to fatigue prediction in the presence of cracks or defect was created by Kitagawa and Takahashi, who developed an eponymous diagram to indicate failure conditions. Kitagawa & Takahashi tested several specimens with different defect areas and observed that the specimen with longer crack sizes has lower fatigue strength [30]. Their schematically experimental data are indicated in black in Fig. 2.13. Smith has estimated two threshold lines for short and long cracks, respectively, which are illustrated in Fig. 2.13 as blue lines [31] by using $\Delta\sigma_0$ and $\Delta K_{th,lc}$. If the specimens are subjected to cyclic loading, a threshold value can be plotted in the logarithmic Kitagawa-Takahashi diagram. At loading above this threshold, crack propagation will take place and eventually leads to completely failure of specimen. Below this data which represent experimentally determined fatigue limit, no failure will be observed. Although short cracks can form, they will be arrested at microstructure barriers, and are known as non-propagating cracks. When the cracks are in the scale of microstructural short cracks, this curve has a horizontal course defined by the fatigue limit of smooth specimens $\Delta\sigma_0$. As the size of the cracks become larger, the threshold curve will decrease more and more rapidly.

Finally, when the crack size progresses sufficiently, the threshold curve approaches the threshold stress intensity factor range for long cracks, $\Delta K_{th,lc}$, which is constant for a given material and load ratio. A more realistic description of the threshold curve has been reported by El Haddad et al., which is illustrated as an orange line in Fig. 2.13. The crack length a is extended by a so-called intrinsic crack length. The threshold value for the crack extension can then be estimated using the following equation:

$$\Delta\sigma = \frac{\Delta K_{th}}{\sqrt{\pi \cdot (a + a_0^*) \cdot Y}} \quad (2-8)$$

The intrinsic crack length, a_0^* , can be calculated as follow equation:

$$a_0^* = \frac{1}{\pi} \cdot \left(\frac{\Delta K_{th}}{\Delta\sigma_0} \right)^2 \quad (2-9)$$

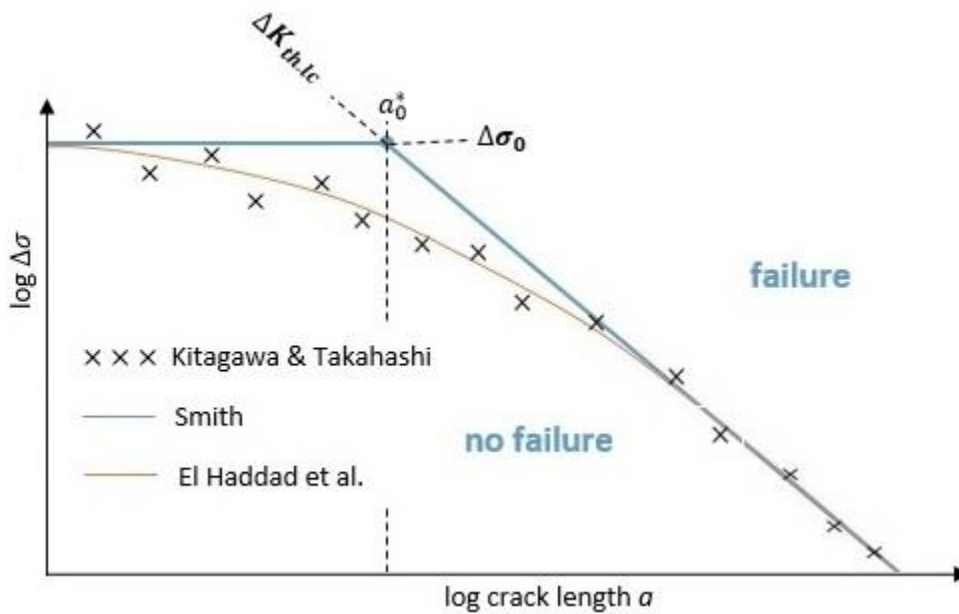


Fig. 2. 13: Kitagawa-Takahashi diagram

2-1-9 \sqrt{area} parameter mode I

Another method to predict the fatigue limit in the presence of short cracks or small defects was developed by Murakami and Endo [18]. Finding a predictive method to determine the fatigue limit, σ_w , as well as threshold stress intensity factor range, ΔK_{th} , for different materials with small defect has always been a challenge for scientists. Murakami and Endo have presented a simple

and useful method, based on only two basic quantities for the prediction of both ΔK_{th} and σ_w for materials containing small defects and cracks [18]. These two parameters are the Vickers hardness, HV , and the material's representative and \sqrt{area} as the geometrical representative parameter. \sqrt{area} is defined as the square root of the area obtained by projecting a small defect or crack onto a plane perpendicular to the maximum principle stress [23] (see Fig. 2.14).

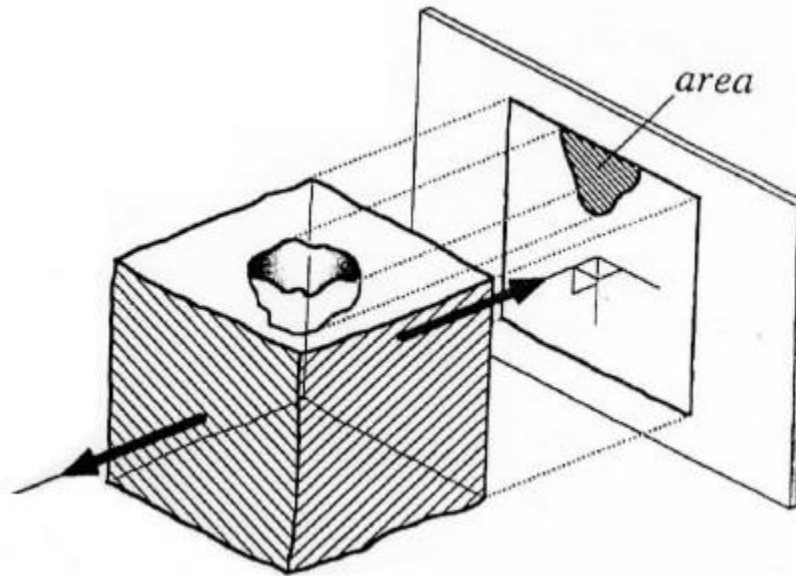


Fig. 2. 14: Definition of \sqrt{area} [23].

After several experiments on different materials with different defects, Murakami has developed the relationship between ΔK_{th} and HV and \sqrt{area} as shown in equation [23]:

$$\Delta K_{th} = 3.3 \cdot 10^{-3} (HV + 120) (\sqrt{area})^{1/3} \quad (2-10)$$

Where ΔK_{th} is in $MPa\sqrt{m}$, \sqrt{area} is in μm and HV is in kgf/mm^2 .

The connection between the threshold SIF range, ΔK_{th} , and the fatigue limit stress range, $\Delta\sigma_w$, can be made with the following formula, which is based on a linear-elastic fracture mechanics analysis [23]:

$$K_{I_{max}} = 0.65 \cdot \sigma_0 \cdot \sqrt{\pi \sqrt{area}} \quad (2-11)$$

In which, the $K_{I_{max}}$ is denoted for the maximum value of the stress intensity factor along the cracks in $MPa\sqrt{m}$ and σ_0 is represented for the applied uniform remote tensile stress in MPa.

Combining Eqs. 2-10 and 2-11, by setting $K_{I\max} = \Delta K_{th}/2$ and $\sigma_0 = \Delta\sigma_w/2$, the fatigue limit, σ_w , of a specimen with a defect can be calculated as follows:

$$\sigma_w = \frac{1.43(HV + 120)}{(\sqrt{area})^{1/6}} \quad (2-12)$$

Where σ_w is in MPa, $\Delta K_{th,lc}$ is in $\text{MPa}\sqrt{\text{m}}$ and \sqrt{area} is in μm .

Murakami has determined that the \sqrt{area} parameter is valid for defects sizes up to approximately 1 mm [32]. However, Chapatti has demonstrated that the maximum size of defects for which the \sqrt{area} parameter mode I is applicable depends on the material [33]. For large defects or long cracks, the value of ΔK_{th} becomes constant, which means that the value of the threshold stress intensity factor range of a long cracks, $\Delta K_{th,lc}$, must be applied [34]. Combining the Eq. 2-10 and $\Delta K_{th,lc}$, the transition size, \sqrt{area}_{trans} (in μm), can be calculated as follow:

$$\sqrt{area}_{trans} = \left(\frac{\Delta K_{th,lc}}{3.3 * 10^{-3}(HV + 120)} \right)^3 \quad (2-13)$$

Using the Eq. 2-11 and the threshold condition, $\Delta K_{th,lc}$, the fatigue limit for large defects can be estimated as follow:

$$\sigma_w = \frac{\Delta K_{th,lc}}{2 * 0.65\sqrt{\pi\sqrt{area}} * 10^{-6}} = 434 * \frac{\Delta K_{th,lc}}{(\sqrt{area})^{1/2}} \quad (2-14)$$

Where σ_w is in MPa, $\Delta K_{th,lc}$ is in $\text{MPa}\sqrt{\text{m}}$ and \sqrt{area} is in μm .

Fig. 2.15 schematically illustrates the fatigue limit prediction lines for short and long cracks. For short cracks the prediction line is plotted according to \sqrt{area} mode I (Eq. 2-12). Prediction line for long cracks beyond the \sqrt{area}_{trans} is plotted according to Eq. 2-14.

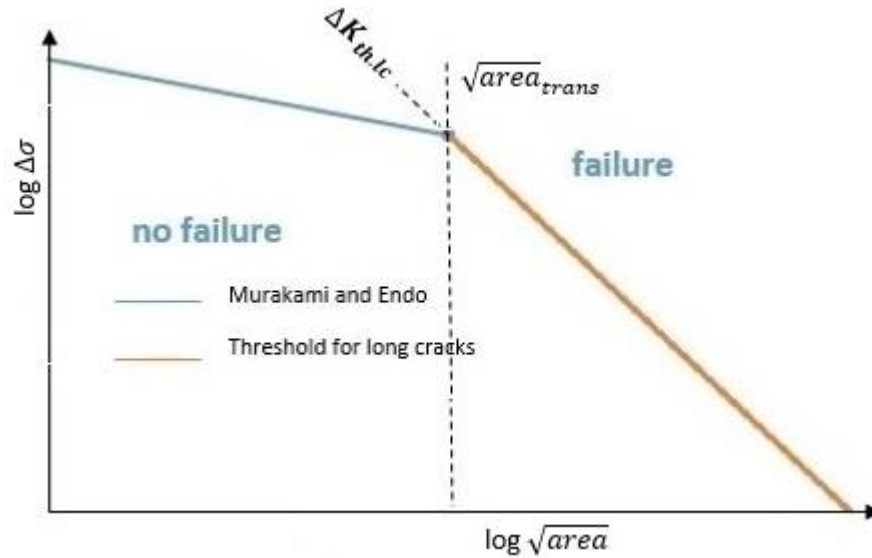


Fig. 2. 15: Murakami and Endo line prediction.

The \sqrt{area} parameter mode I has been discussed in many previous works related to uniaxial fatigue strength (e.g.[35],[23]). The extended application of this mode I to multiaxial fatigue problems, i.e. torsional loading, has been discussed by Endo [36]. After a critical size, the fatigue crack is likely to propagate perpendicular to the major principal stress direction. Considering the major and minor principal stresses σ_1 and σ_2 , the fatigue limit can be calculated by the following equation:

$$\sigma_1 + k\sigma_2 = \sigma_w = \frac{1.43(HV + 120)}{(\sqrt{area})^{1/6}} \quad (2-15)$$

Where k is a parameter that accounts for the influence of stress biaxiality. To calculate Eq. 2-15 for torsional loading, as shown in Fig. 2.16 by a transformation to principal stresses, we have $\sigma_1 = \tau$ and $\sigma_2 = -\tau$. So by rewriting Eq. 2-15 for torsional loading, we reach the following equation:

$$\tau_w = \left(\frac{1}{1-k} \right) * \frac{1.43(HV + 120)}{(\sqrt{area})^{1/6}} \quad (2-16)$$

The effect of biaxial stress, k , is various for different materials. $k = -0.18$ was reported for carbon steel and Cr-Mo steel [37]. For 17-4PH stainless steel, it was found to be $k = 0$. If the effect of

biaxial stress is negligible (i.e., $k = 0$), the torsional fatigue limit, τ_w , is determined by following equation:

$$\tau_w = \frac{1.43(HV + 120)}{(\sqrt{area})^{1/6}} = \sigma_w \quad (2-17)$$

Furthermore, for the case of $\sqrt{area} > \sqrt{area}_{trans}$, the torsional fatigue limit can be calculated as following equation:

$$\tau_w = \frac{\Delta K_{th,lc}}{2 * 0.65\sqrt{\pi\sqrt{area}} * 10^{-6}} = 434 * \frac{\Delta K_{th,lc}}{(\sqrt{area})^{1/2}} = \tau_w \quad (2-18)$$

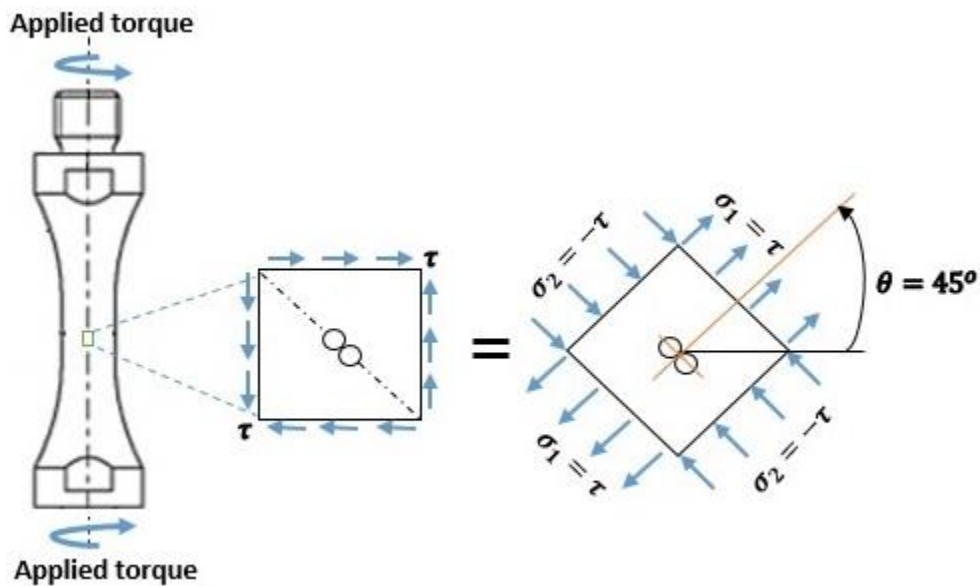


Fig. 2. 16: Stress transformation on the specimen surface.

2-2 Stainless steel

Stainless steel is an iron-based alloy with significant chromium content. Chromium produces a thin layer of oxide on the surface of the steel known as the 'passive layer'. This prevents any further corrosion of the surface. Increasing the amount of chromium gives an increased resistance to corrosion. In many cases, other special chemical elements added in addition to chromium, including nickel and molybdenum. As mentioned above, the main characteristics of this family of steels is resistance to wet or electrochemical corrosion in aggressive environments such as fresh

water, sea water, contaminated water-based solutions, acid and base environments, industrial environments, etc. Another important characteristic of this category of steel is the resistance to oxidation at high temperatures which typically occurs in hot process gases. The typical fields of application for stainless steel are in the chemical, oil, foodstuffs, paper manufacturing, pharmaceuticals, biomedical, and transport sectors. On the basis of their main microstructural features, stainless steels may be organized into the following categories:

Ferritic stainless steels: These steels are based on chromium with small amounts of carbon; usually less than 0.10%.

Martensitic stainless steel: These steels are similar to ferritic steels in being alloyed primarily with chromium (between 12 and 17 wt.%), but have carbon levels as high as 1%. This allows them to be hardened and tempered much like carbon and low-alloy steels. They are used where high strength and moderate corrosion resistance is required.

Austenitic stainless steels: These alloys contain 18 wt.% chromium and 8 wt.% nickel. The nickel balances the effects of the chromium and stabilizes the austenitic phase, as well as makes the alloy more expensive than martensitic variants.

Chapter 3

Materials and test procedure

3-1 Testing material

The testing material used was a chromium-nickel-copper stainless steel 17-4PH, precipitation hardened at 621°C for 4 h. Precipitation-hardened chromium-nickel-copper stainless steel 17-4PH possesses high strength and toughness, as well as good corrosion resistance [15]. Therefore, it is widely used in applications where these properties are required, e.g., in the aerospace, chemical, food-processing industries. Also for biomedical devices such as hand tools and surgical staplers, the 17-4PH steel is interesting due to the combination of high strength and good corrosion resistance. The chemical composition and mechanical properties are given in tables 3.1 and 3.2 respectively. The martensitic microstructure of 17-4PH is illustrated in Fig. 3.1.

Table 3. 1: Chemical composition of the 17-4PH in weight %.

| C | Si | Mn | Cr | Cu | Ni | Nb + Ta | P | S |
|-------|------|------|-------|------|------|---------|-------|-------|
| 0.033 | 0.40 | 0.49 | 15.57 | 3.31 | 4.37 | 0.23 | 0.027 | 0.001 |

Table 3. 2: Mechanical properties of the 17-4PH at room temperature.

| Tensile strength (MPa) | Yield strength (MPa) | Elongation (%) | Reduction of area (%) | Vickers hardness (kgf/mm ²) |
|------------------------|----------------------|----------------|-----------------------|---|
| 1030 | 983 | 21 | 61 | 352 |



Fig. 3. 1: Martensitic microstructure of 17-4PH [15].

Non equilibrium solidification or inappropriate chemical components can lead to form the delta ferrite composition among the martensitic structure of stainless steel. To distinguish the existence of delta ferrite structure, the etching method can be applied. The specimens have undergone stainless steel etching procedures for delta ferrite as describe in literature [38]. The etch is composed of 20 g of NaOH in 100 ml of distilled water. The specimens were etched by applying a voltage of 3 V for 15 s. Fig. 3.2 illustrates the surface of the specimens after etching as seen under an optical microscope. It is obvious in Fig. 3.2 that the delta ferrite grains are elongated in rolling direction.

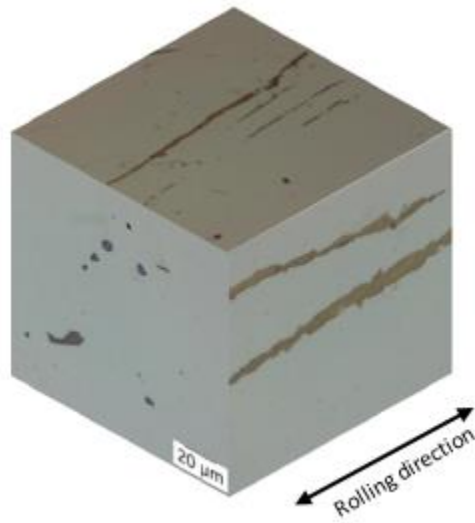


Fig. 3. 2: Orientation of delta ferrite grains. (visible after etching in 20% NaOH)

3-2 Specimen shape and preparation

For the ultrasonic fatigue experiments, two types of shape were investigated. The first was a cylindrical shape with a diameter of 4mm (see Fig. 3.3a), and the second was an hourglass shape (see Fig. 3.3b).

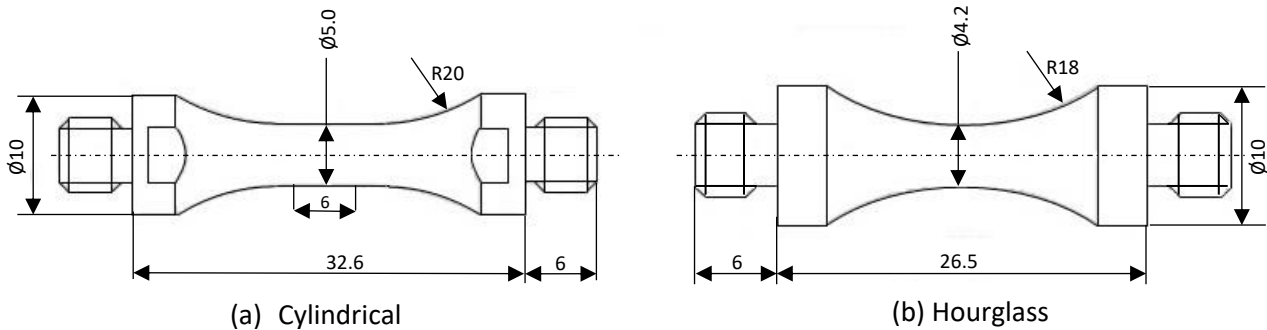


Fig. 3. 3: (a) Cylindrical and (b) hourglass specimen for torsion fatigue test.

Furthermore, the Fig. 3.4 illustrates the geometry of the specimens which are used in servohydraulic test equipment. Servohydraulic fatigue tests were performed at Fukuoka University, Japan (Ref. [39]), and the results are compared with the data measured in the frame of this thesis.

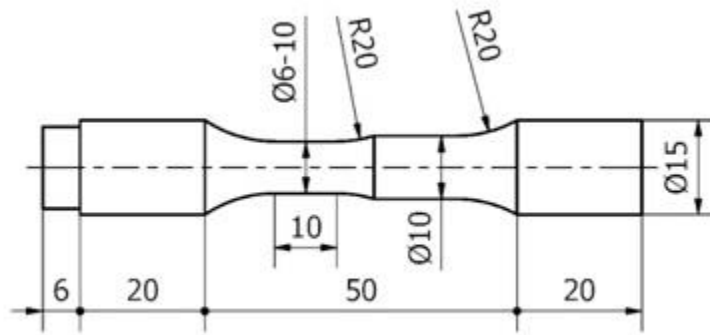


Fig. 3. 4: Geometry of servohydraulic fatigue test specimen [17].

To avoid any micro scratches, the surface of the specimens was ground with four different grades of emery paper (grade 500-2500). On average, the grinding removed about $20 \mu\text{m}$ from the diameter of the specimen. In addition, the specimens were electropolished for 30 minutes (see Fig. 3.5), which take away about $70 \mu\text{m}$ from the diameter. To remove the equal amount of material during the electropolishing, the specimens were rotated through the procedure. The liquid used in electropolishing consisted of 1 l phosphoric acid, 33 g of oxalic acid, and 33 g of gelatin. The end shape of the specimens is shown in Fig. 3.6.



Fig. 3. 5: Equipment for electropolishing.



Fig. 3. 6: End shape of specimens.

In order to investigate the defect tolerance of stainless steels, artificial drilled holes (1-hole, 2-hole and 3-hole) were introduced in the gage length of the specimens with the high precision drill machine illustrated in Fig. 3.7.



Fig. 3. 7: Micro drill machine.

To remove residual stresses that might have been introduced during drilling, the samples were heated in a high vacuum (10^{-6} mbar) over one hour from room temperature to 600°C, and then

held at this temperature for another hour. The temperature was then lowered to 400°C at a cooling rate of 100°C/h (see Fig. 3.8). The final cooling to room temperature was carried out without regulation over about 12 hours. In order to ensure consistent material properties, also smooth specimens were stress relief annealed in the same way.



Fig. 3. 8: Oven and centrifuge pump used for residual stress relieving.

The orientation and the dimension of the holes are shown schematically in Fig. 3.9 and Fig. 3.10.



Fig. 3. 9: The orientation of difference holes.

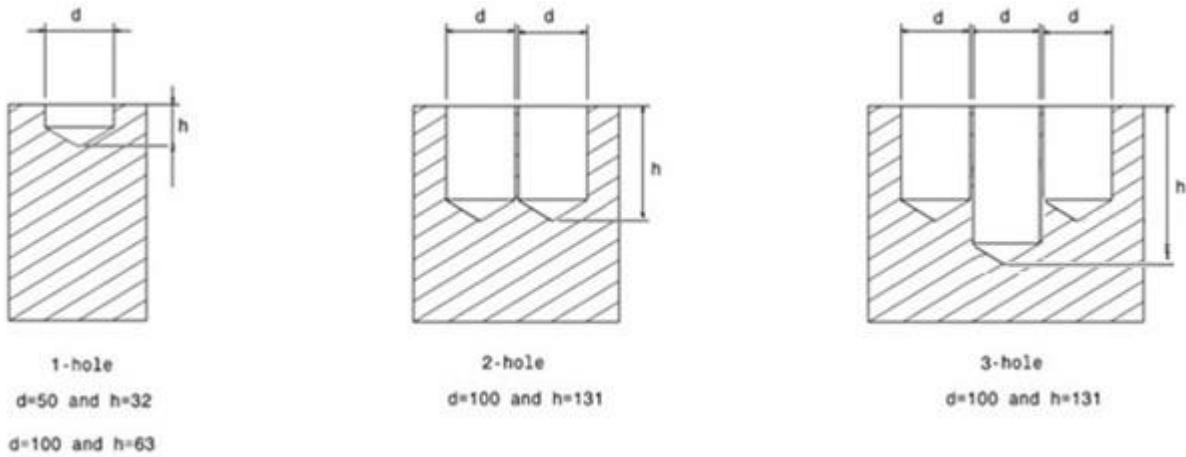


Fig. 3. 10: Dimension of artificial drilled holes in μm .

3-3 Ultrasonic fatigue testing equipment

To perform the fatigue tests, an ultrasonic fatigue system was used. This test system generates a sinusoidal oscillation under resonance conditions at a natural frequency of about 20 kHz. Piezoelectric ultrasonic converters generating push-pull resonance vibrations are used in most ultrasonic fatigue studies, where the specimens are subjected to cyclic axial loading with the principal stress directed along the length of the specimen. The ultrasonic fatigue testing method is not restricted to cyclic axial loading, however. Mayer et. al developed a method to investigate the fatigue properties of materials under ultrasonic torsion resonance loading [40]. In torsional loading, the piezoelectric converter transforms the sinusoidal power signal into mechanical twisting oscillations of about 20 kHz and injects longitudinal waves into one end of the load train. If the frequency of the electric power signal to drive the ultrasonic converter and the mechanical resonance frequency of the load train coincide, the vibration amplitude can reach the necessary magnitude to perform fatigue experiments. In this situation, the specimens' ends twist in opposite directions and a vibration node is formed in the center, where cyclic shear loading leads to crack initiation and fatigue fracture. Fig. 3.11 illustrates the mechanical components of ultrasonic fatigue testing under torsional loading, which was developed at BOKU University [14]. The ultrasonic converter (1) transforms sinusoidal electric power into mechanical oscillations. The upper mounting part (2) transfers the vibration into the load train with the same frequency vibration. The ultrasonic titanium horn (3) magnifies the vibration amplitude along the load train by decreasing the diameter of the titanium horn along its length. The specimen (5) is mounted at one end of the

titanium horn (3 and 6). To measure the maximum cyclic strain, the strain gauges are adhered in the center area of the specimens. To control the experiments, the vibration gauges (4) measure the vibration amplitude at the titanium horn close to one specimen's end. To keep the specimen's temperature within a limited range, the cyclic load is performed in pause and pulse form and cooling air is used. To perform the ultrasonic fatigue test with higher stress ratio, the static torsion load can be superimposed to the ultrasonic torsion vibration. To produce a specified static torque, the static load is applied to the lower mounting part and rotating disc (7). By changing the applied force, the desired stress ratio can be obtained.

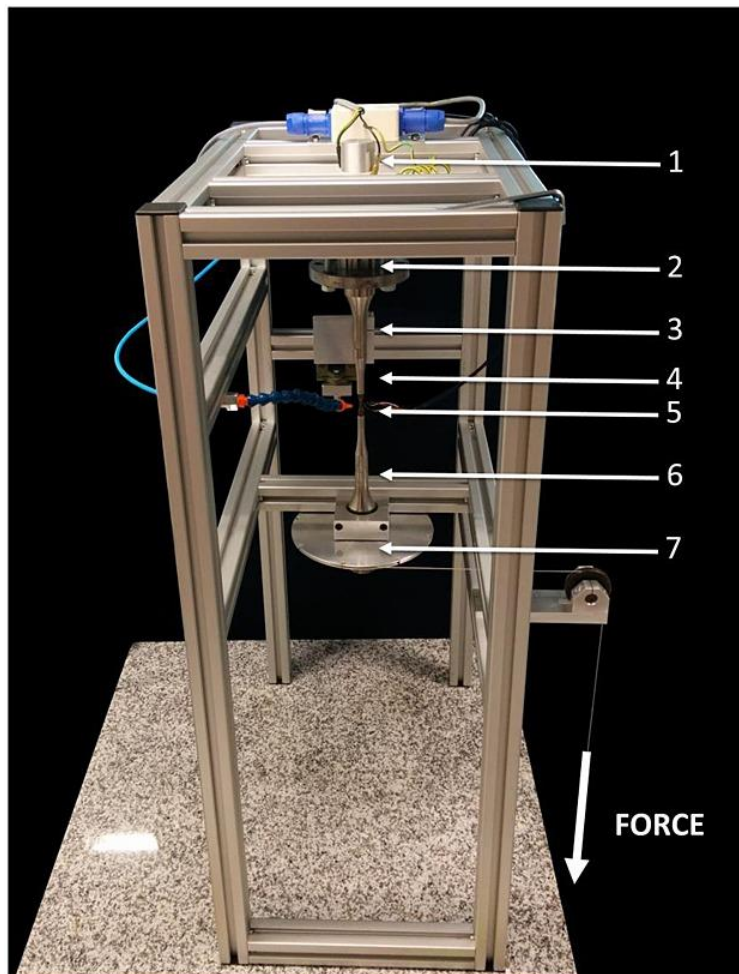


Fig. 3. 11: Mechanical setup and load train for ultrasonic cyclic torsion tests: (1) ultrasonic converter, (2) upper mounting part, (3) and (6) ultrasonic horns, (4) vibration gauge, (5) specimen and (7) rotating disc and lower mounting part [15].

Chapter 4

Results and discussion

4-1 Smooth specimens with $R = -1$

The $S-N$ data of smooth specimens without any superimposed load at $R = -1$, achieved from ultrasonic fatigue testing under torsional loading conditions in frequency of 20 kHz in ambient air are summarized (see Fig. 4.1 and 4.2). In Fig. 4.1 the cylindrical and in Fig. 4.2 the hourglass specimens are shown. Shear stress amplitudes, τ_a , which are half of the respective stress ranges, $\Delta\tau$, are used as ordinate. Stresses are calculated using the measured shear strain amplitudes at the beginning of the experiments, as well as the shear modulus. The specimens that underwent at least 10^9 cycles without any failure are shown with an open circle and called runout specimen.

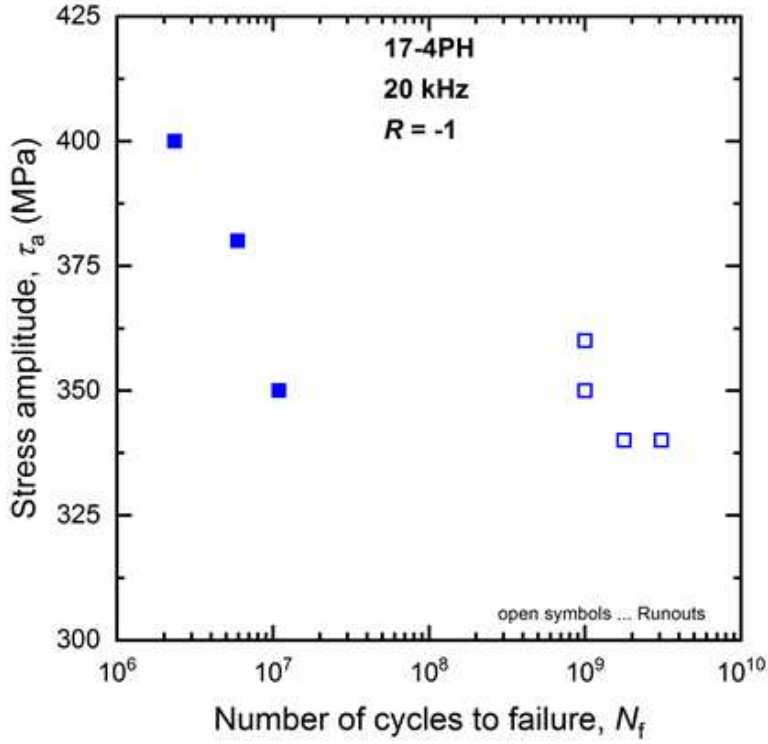


Fig. 4. 1: S-N diagram of smooth cylindrical specimens under torsional loading at $R = -1$.

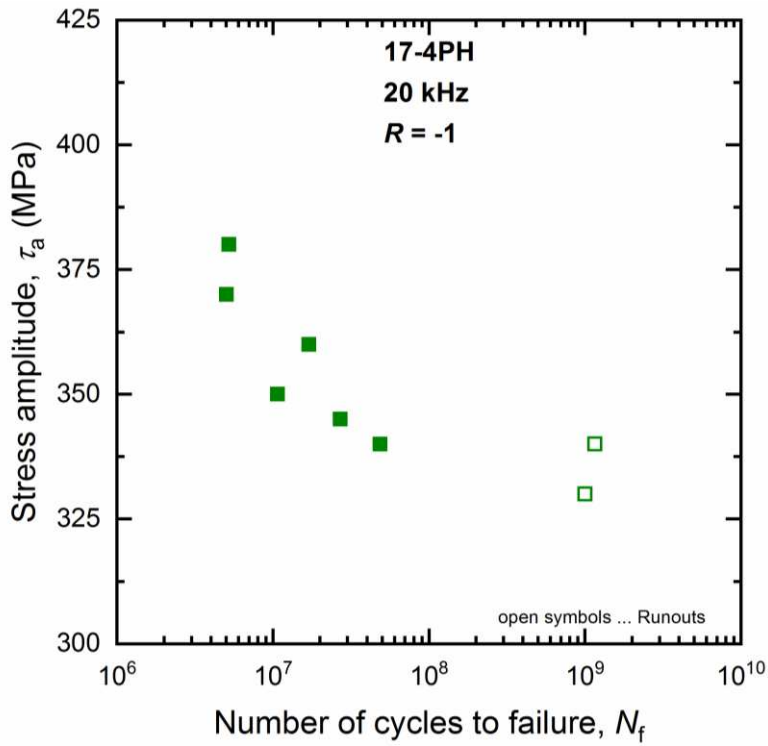


Fig. 4. 2: S-N diagram of smooth hourglass specimen under torsional loading at $R = -1$.

The surface of specimens are observed with optical microscopy after testing. Fig. 4.3 shows locations of crack initiation. It can be seen that crack initially initiate under Mode II/III and continue propagation under Mode I after crack branching. The orientation of Mode II/III cracks can be both horizontal and vertical. It should be noted that non-propagating cracks were not observed on the surface of runout spesimens.

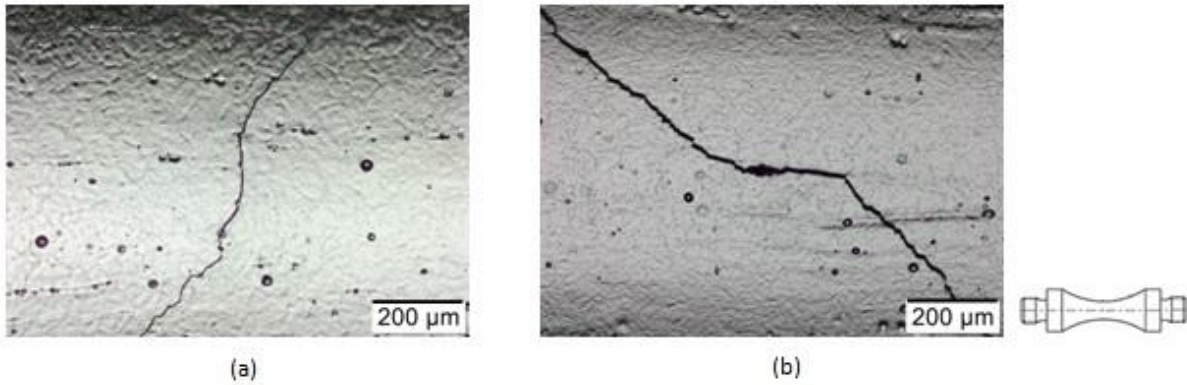


Fig. 4. 3: Fatigue cracks growth in smooth specimens under torsional loading at $R=-1$ and (a) $\tau_a = 340$, $N_f = 4.8 \times 10^7$
(b) $\tau_a = 345$, $N_f = 2.7 \times 10^7$.

4-1-1 Influence of specimen shape

As mentioned above, cylindrical and hourglass shaped specimens were tested. Fig. 4.4 summarizes the result of both shapes in one plot. It is obvious that there is no significant variation in fatigue lifetimes between the two specimen shapes.

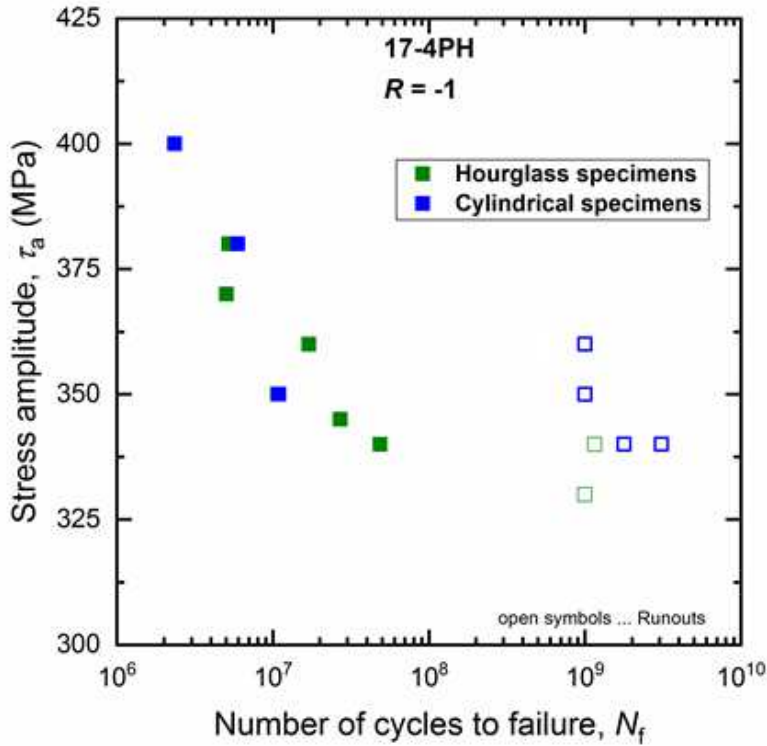


Fig. 4. 4: Comparison of S-N data between smooth cylindrical and hourglass specimen at $R=-1$.

4-1-2 Influence of loading direction

The results from smooth specimens under torsional ultrasonic fatigue testing are compared to tension-compression ultrasonic fatigue testing in Fig. 4.5 (tension-compression results from Ref. [41]). In previous investigations, it has been shown that the tension-compression fatigue limit of smooth specimens, σ_{w0} , can be predicted effectively using the simple estimation $\sigma_{w0} = 1.6 \cdot HV$, with a Vickers hardness of $HV = 352$ [41]. Under torsional loading, it has been shown that the fatigue limit, τ_{w0} , correlates closely to the von Mises criterion:

$$\tau_{w0} = \frac{\sigma_{w0}}{\sqrt{3}} = 1.6 \cdot \frac{HV}{\sqrt{3}} \quad (4-1)$$

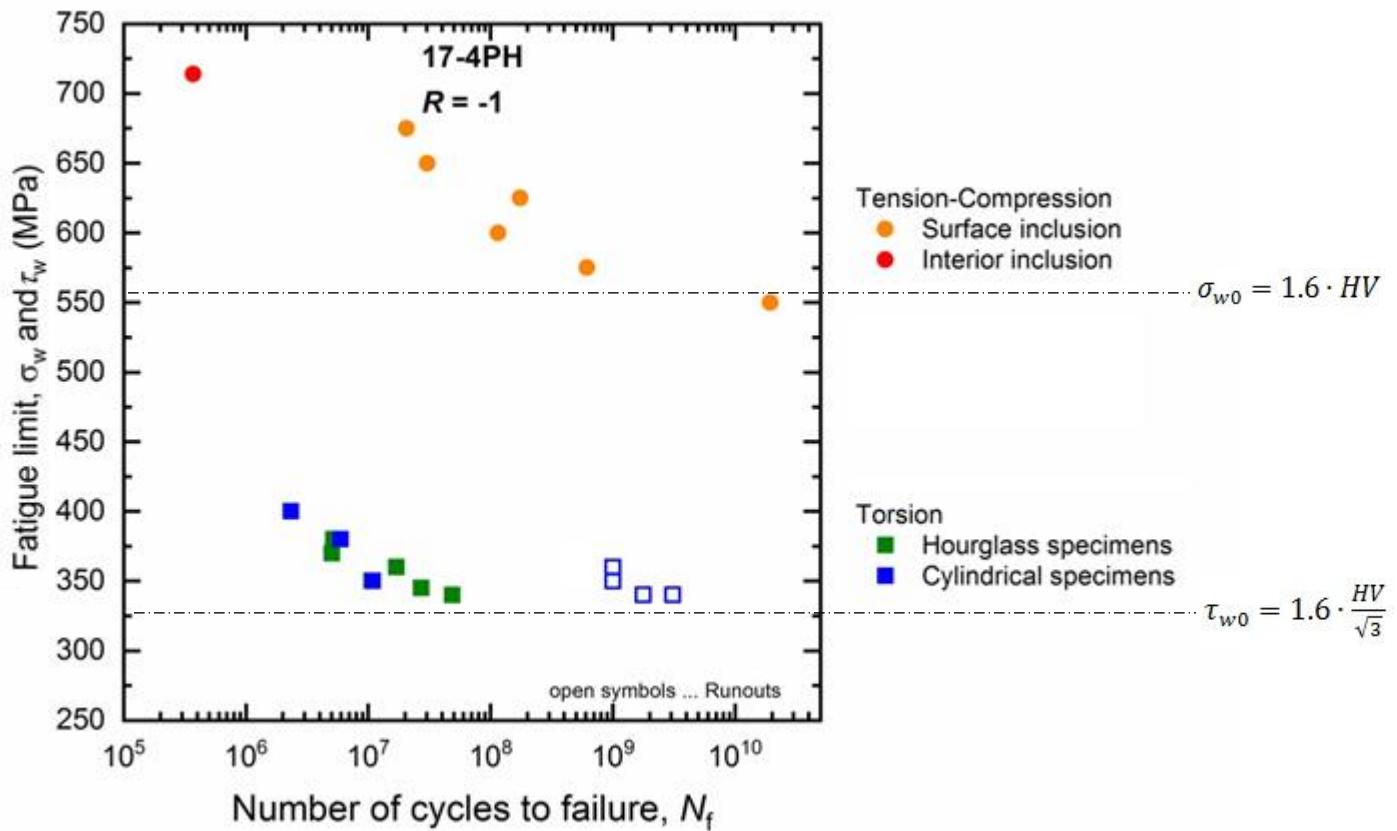


Fig. 4. 5: Relationship between fatigue limit in smooth specimens under uniaxial and torsional loading condition [42].

Schönbauer et al. have determined that in a uniaxial fatigue test, cracks nucleate from inclusions [15]. The cracks can initiate either from the interior or surface of the material. Fig. 4.6 illustrates the position where fatigue cracks were nucleated under uniaxial loading. In Fig. 4.6a, the crack was initiated from a surface inclusion, but in Fig. 4.6b, the crack is nucleated from an interior inclusion. In contrast, under torsional loading, it can be observed that all specimens failed from the surface and no inclusions were observed at the crack initiation sites. Fig. 4.7 shows the positions of crack nucleation in torsional fatigue loading in two smooth specimens.

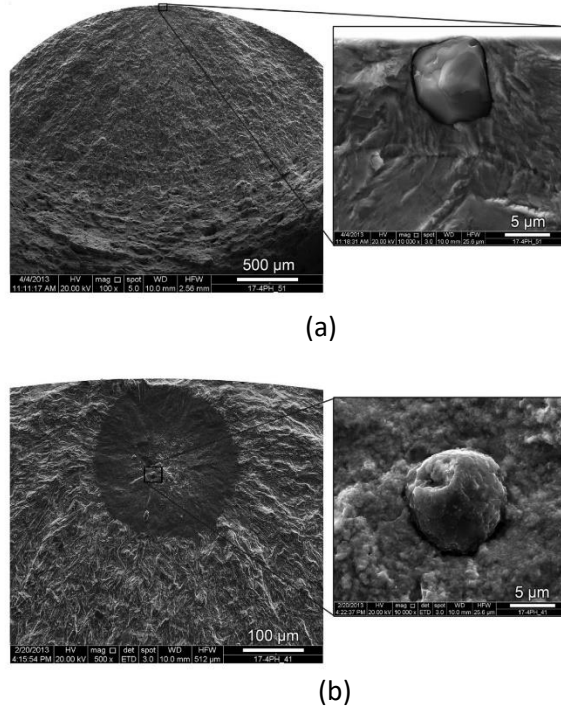


Fig. 4. 6: Crack initiation site under uniaxial loading at (a) surface inclusion and (b) Internal inclusion [34].

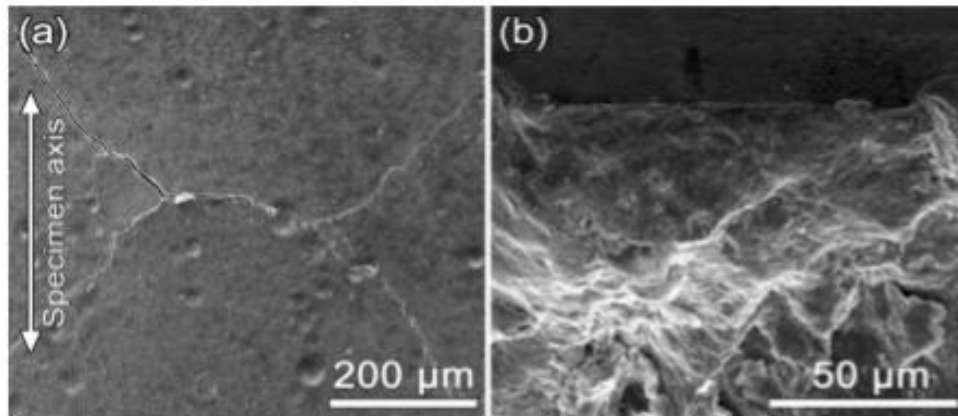


Fig. 4. 7: Crack initiation site under torsional loading [42].

4-2 Influence of frequency

In this study, 20 kHz ultrasonic fatigue testing was used solely. Schönbauer et al. [39] performed fatigue tests with the same material with conventional servohydraulic fatigue testing equipment (MTS equipment) at 25-30 Hz. Fig. 4.8 summarizes the two sets of data.

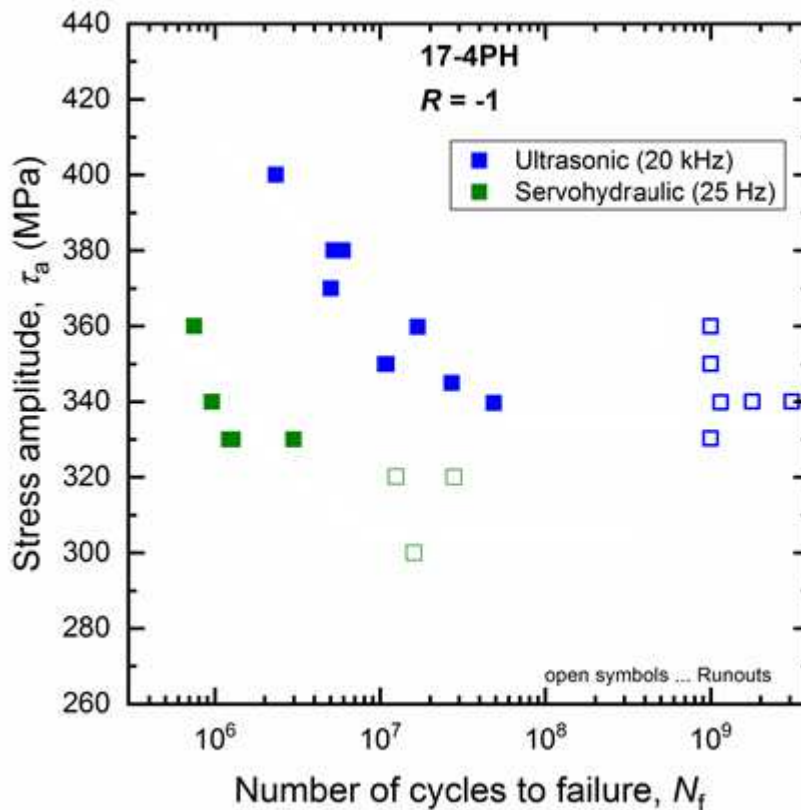


Fig. 4. 8: Influence of different frequency on fatigue strength of specimens.(Data for servohydraulic testing from Ref.[41])

The $S-N$ curves show that the fatigue lifetimes increase as the frequency applied by the test equipment increases, which suggests a frequency effect as, for example, reported by Tsutsumi et al. (e.g. [43]). However, under uniaxial loading, no frequency effect was found for the same testing material [15]. Specimens that were tested at 25 Hz as reported in Ref. [39] were investigated by light microscope. Fig. 4.9 shows non-propagating cracks for a run out specimen. It has to be noted that most mode II/III cracks were initiated in specimens' length direction, and the cracks seem to have initiated at elongated grains.

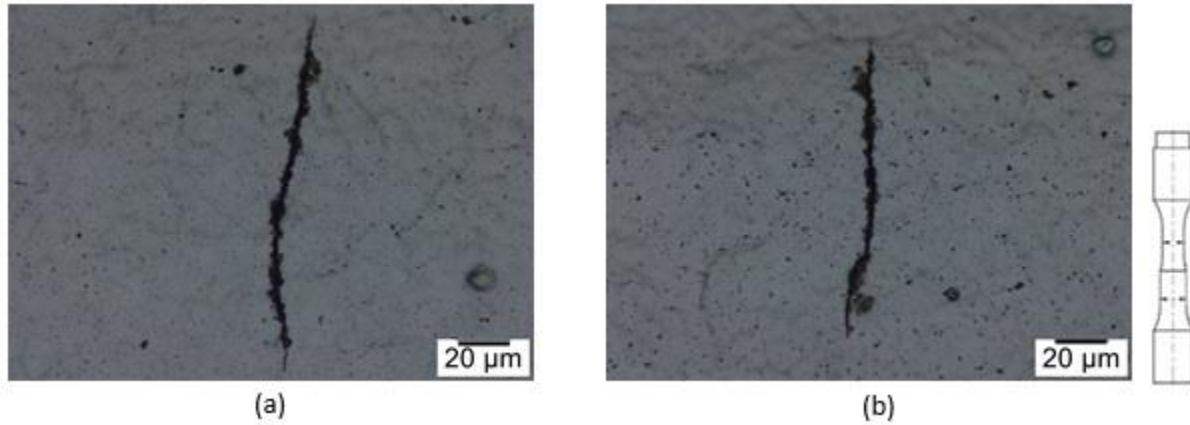


Fig. 4. 9: Non-propagating cracks observed after testing at the frequency of 25 Hz for a runout specimen at $R=-1$, $\tau_a = 320$ and $N_f = 6 * 10^6$

The specimens have undergone stainless steel etching procedures for delta ferrite as describe in section 3.1. Fig. 4.10 illustrates the surface of the specimens after etching as seen under an optical microscope. The orientation of the delta ferrite region is elongated in rolling direction, which is the specimens' length direction.

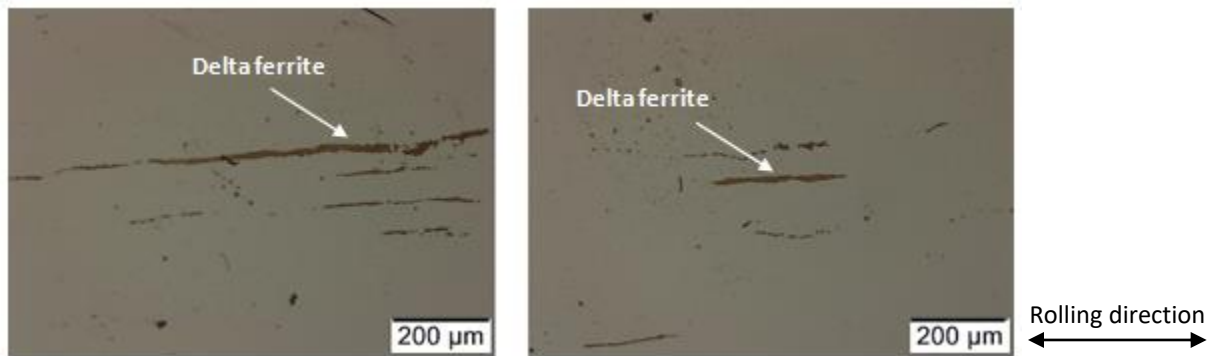


Fig. 4. 10: Surface of specimen after etching and the orientation of delta ferrite grains.

To determine the effect of delta ferrite on fatigue life, the surface of specimens after crack initiation was observed by optical microscopy. Fig. 4.11 shows a failed specimen which has been loaded under conventional servo hydraulic testing equipment at a frequency of 25-30 Hz. As shown in Fig. 4.11b with higher magnification, the cracks have clearly initiated in a δ -ferrite grain. In Fig. 4.12, a non-propagating crack that has formed during low frequency testing is illustrated. After etching, the initiation site along the delta ferrite grain is also obvious in this figure.

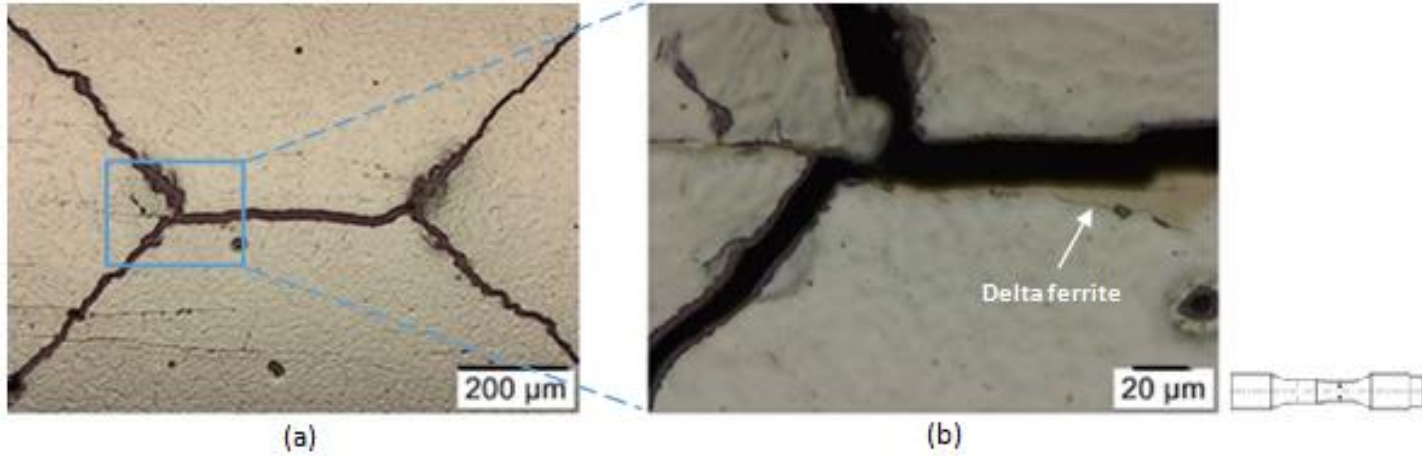


Fig. 4. 11: Crack site in delta ferrite region for specimen under torsional loading at frequency of 25 Hz, $\tau_a = 340$ and $N_f = 9.6 * 10^5$, (a) overview, (b) higher magnification.

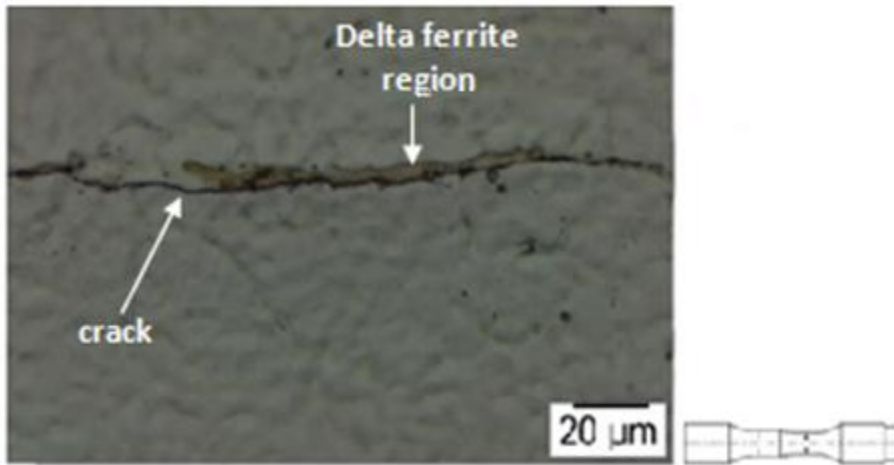


Fig. 4. 12: Non propagating crack in the delta ferrite region at frequency of 25 Hz, $R=-1$, $\tau_a = 330$ and $N_f = 2.9 * 10^6$.

In contrast, Fig. 4.13 illustrates the surface of a specimen subjected to ultrasonic fatigue testing at 20 kHz. Also this specimen has been etched but no δ -ferrite grain could be detected at the crack initiation site. Therefore, the crack has most probably nucleated in the bulk material. The same observation could be made with other failed specimens.

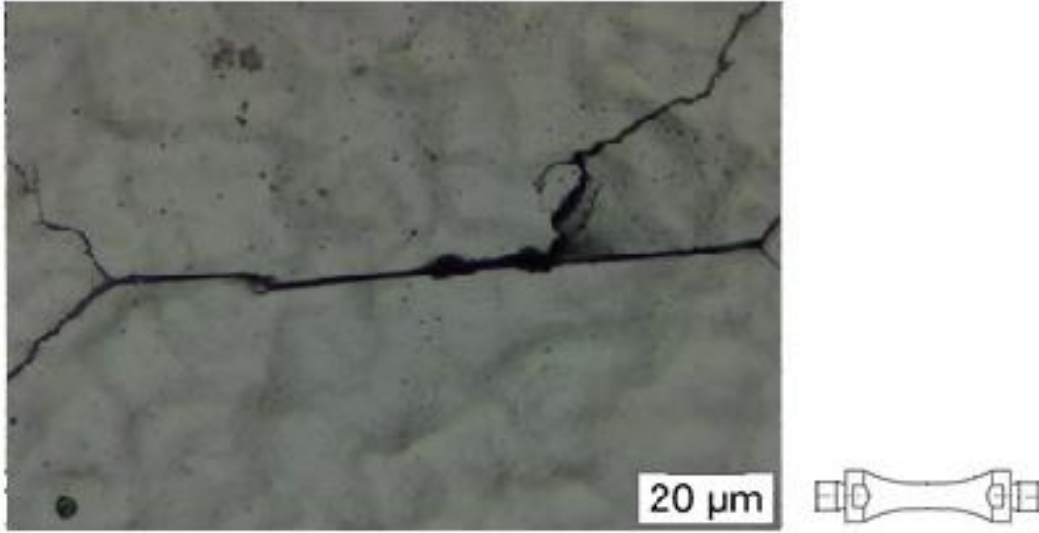


Fig. 4. 13: Etched specimen after cyclic loading in ultrasonic test equipment at frequency of 20 kHz, $\tau_a = 345$ MPa and $N_f = 2.7 * 10^7$.

It has been shown that the presence of delta ferrite decrease both the crack initiation and propagation energy [44]. It can therefore be concluded that increasing the frequency lowers the deleterious effect of delta ferrite content on fatigue strength.

Crack that initiate in delta ferrite grains can obviously cause failure, but they may also arrest. To investigate the shape of non-propagating cracks initiated in delta ferrite grains as well as in the martensitic matrix, a new method similar to that already applied by Endo et al. [45] was applied. A run-out specimen which was tested at the torsional fatigue limit ($\tau_a = 320$ MPa) using servo hydraulic test equipment at a frequency of 20 Hz, was selected. Fig. 4.14 and Fig. 4.15, illustrate the four largest non-propagating cracks on the surface of the specimen that were found during optical investigation. The cracks in Fig. 4.14 are elongated in rolling direction of specimen, which is also the elongation direction of delta ferrite grains. The existence of delta ferrite region around the cracks is clearly visible. In contrast, the both cracks shown in Fig. 4.15 are perpendicular to role direction of specimen and thus, there is no delta ferrite component around these two cracks that formed in the martensitic matrix.

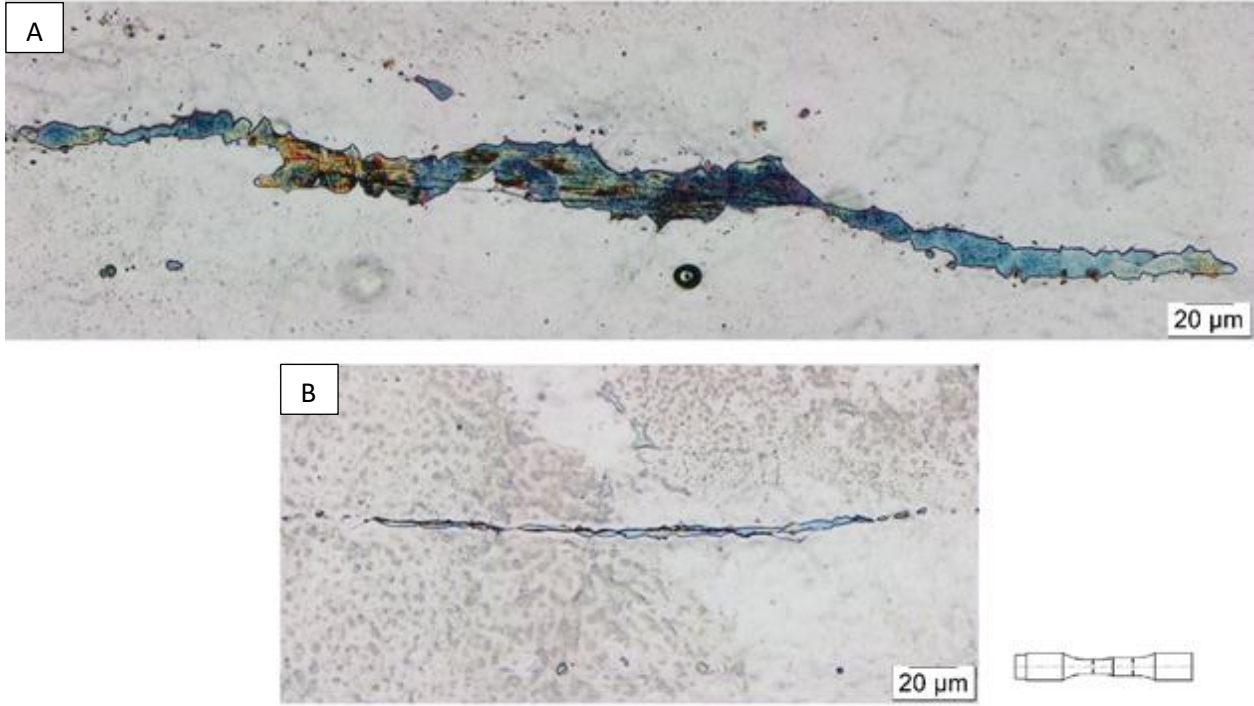


Fig. 4. 14: Non-propagating cracks(A+B) formed at delta ferrite grains elongated in role direction.

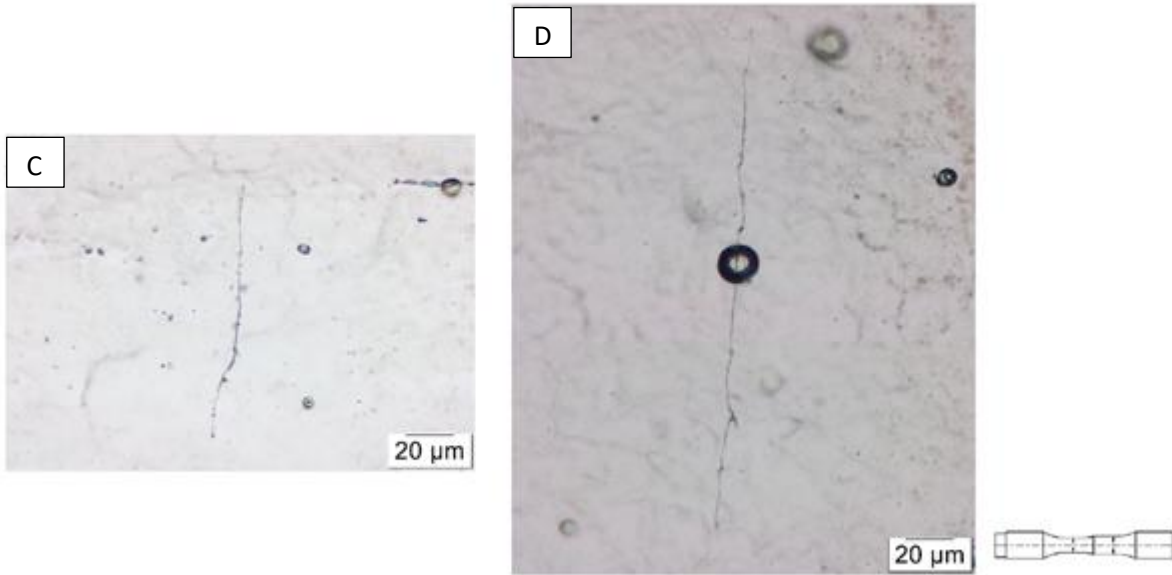


Fig. 4. 15: Non-propagating cracks (C+D) formed in the martensitic matrix with orientation perpendicular to specimen axis.

In order to determine the length and form of the cracks and delta ferrite, the following steps were applied. First of all, as shown in Fig.4.16, the surface of specimen close to the cracks was marked with a Vickers hardness testing machine with different forces and different depths respectively. Afterwards, the surface of specimen was ground for about 30 minute with 1 μm Alumina powder buff solution in each step to remove about 3 μm . With measuring the depth of given indentation before and after the grinding, the exact amount of surface removal in each step can be determined. Furthermore, to make the crack tips better observable, the specimen was electropolished for 8 s, which was short enough not to remove a significant surface layer. In each step, the specimen was etched to color the delta ferrite region after grinding. The form and length of cracks and delta ferrite region were investigated under light microscope and were recorded. The grinding has been continued until no crack and also delta ferrite could be further detected.

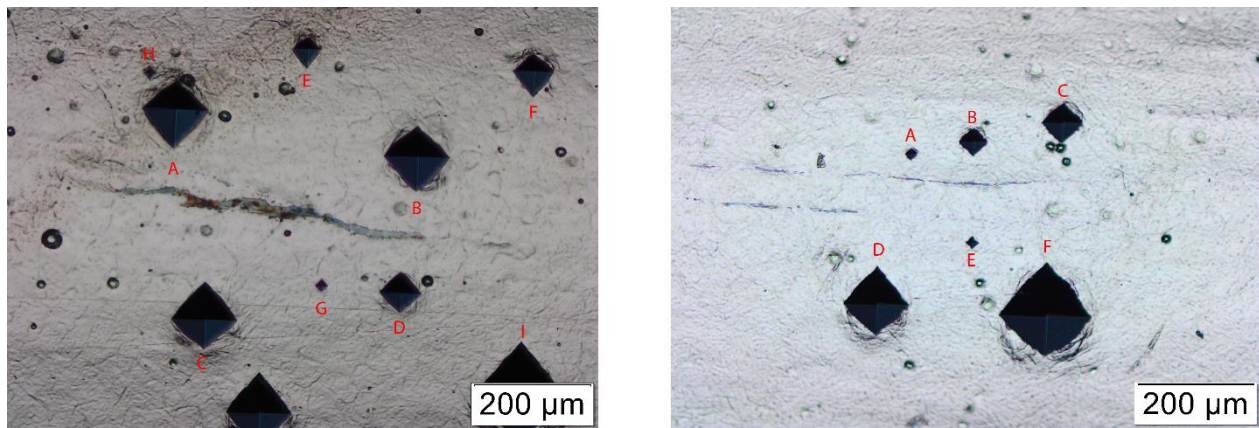


Fig. 4. 16: Indentations close to the crack with Vickers hardness testing machine.

The length and depth of cracks and delta ferrite region inside the specimen are illustrated for cracks A to D in Fig 4.17 till Fig 4.21, respectively. In addition, some images of the cracks that were made for the measurement are illustrated. It can be seen that the cracks which are elongated in delta ferrite direction (for example, crack A and B), initiate from the delta ferrite grains. However, these cracks also can propagate out of the delta ferrite grains (for example see Fig. 4.17 at the depth of 10 μm). But, the depth of crack is in correspondence with the depth of delta ferrite grains.

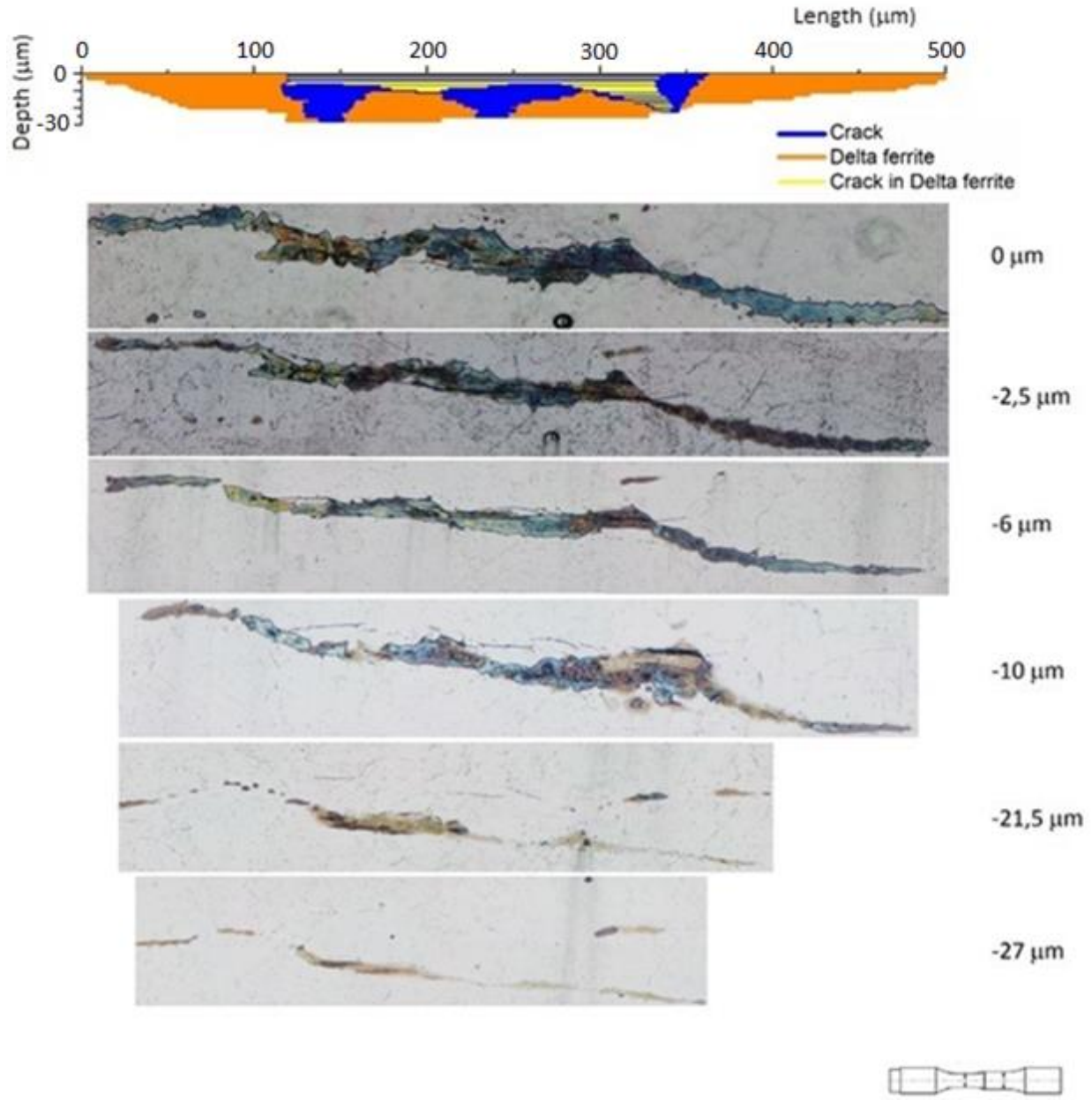


Fig. 4. 17: The form of crack A and the delta ferrite region.

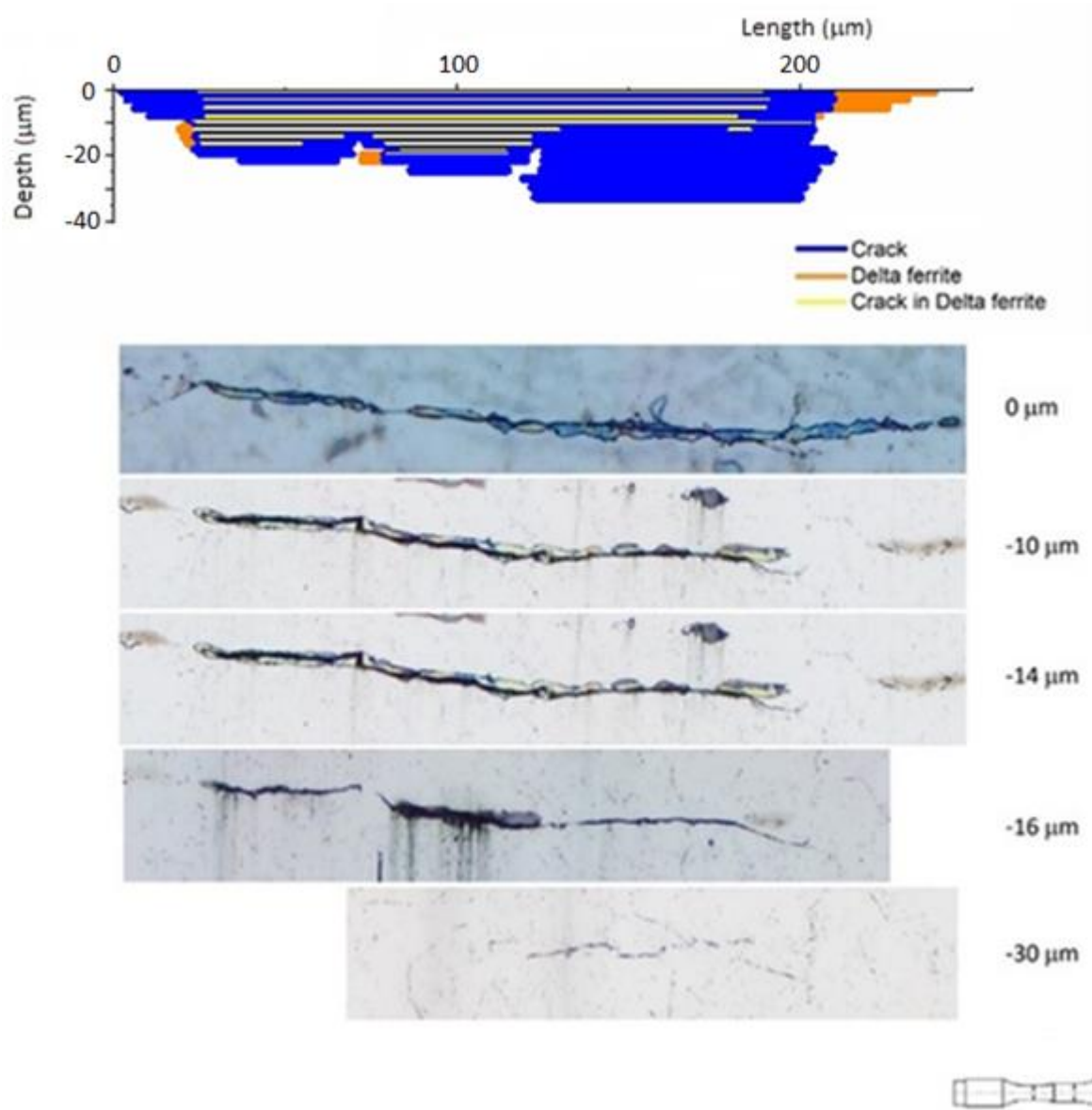


Fig. 4. 18: The form of crack B and the delta ferrite region.

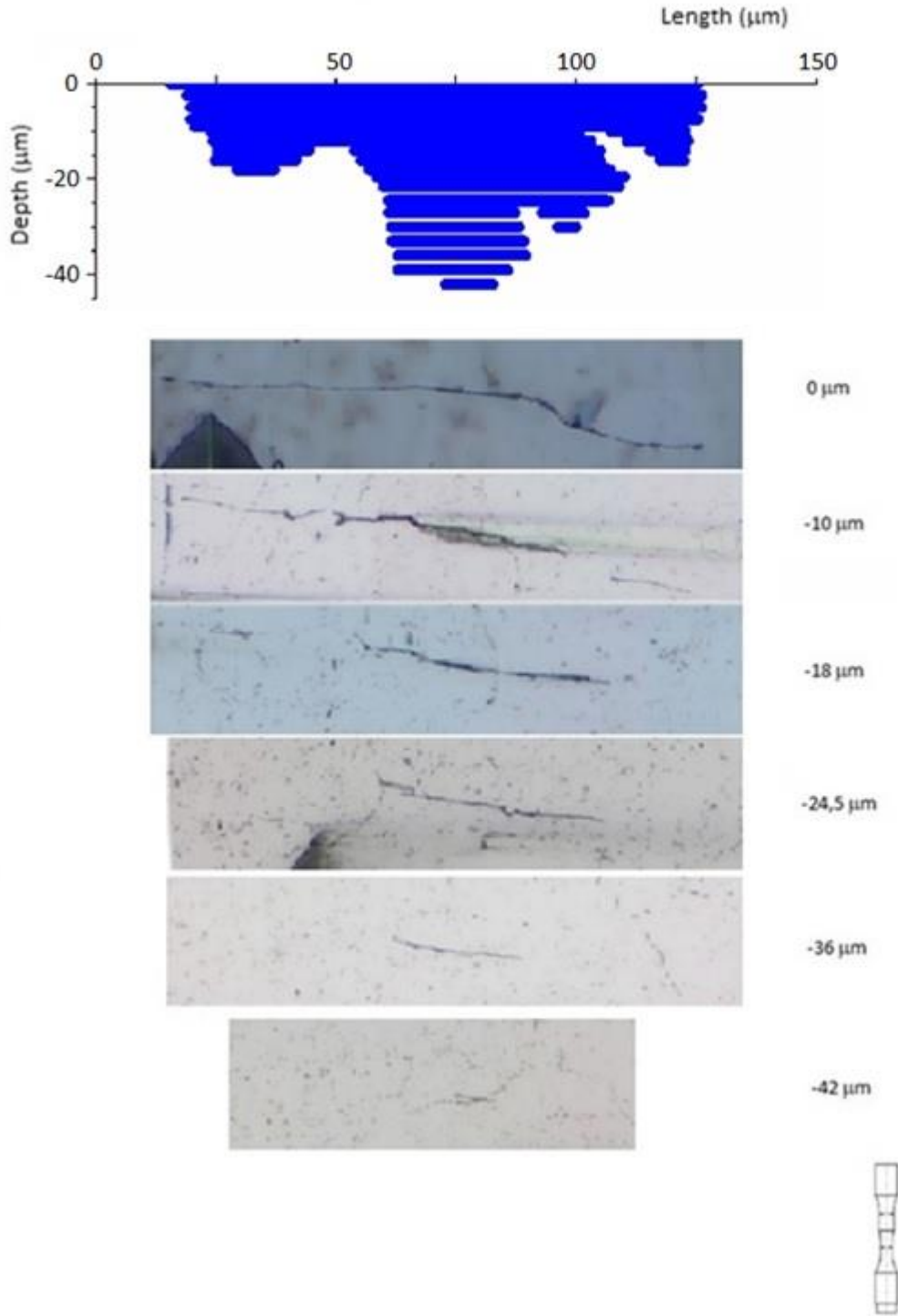


Fig. 4. 19: The form of crack C.

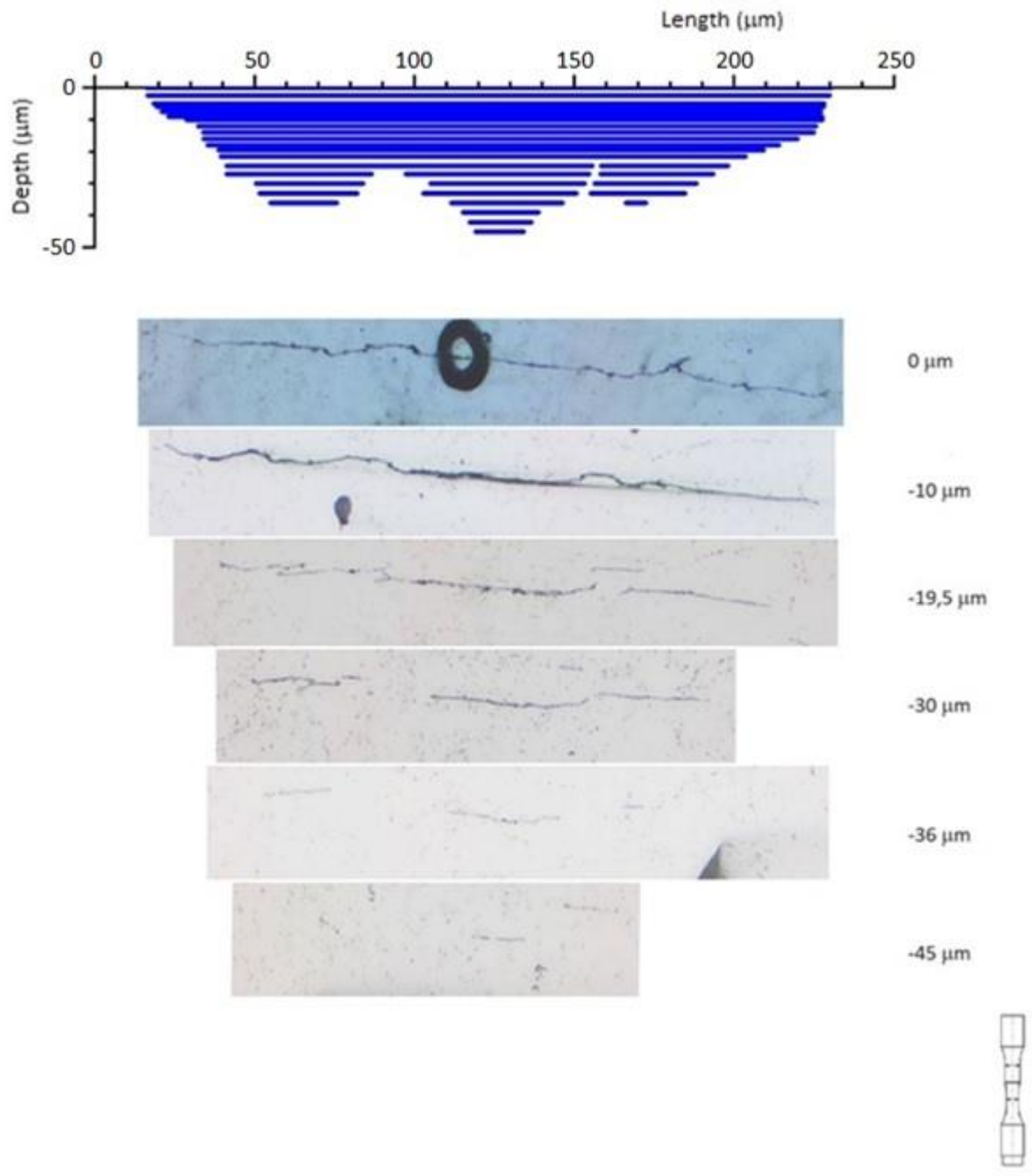


Fig. 4. 20: The form of crack D.

Endo and Yanase demonstrated for annealed carbon steel that the torsional fatigue limit is determined by the macroscopic propagation of a Mode I crack [45]. They assumed that “the fatigue limit corresponds to the threshold stress that can activate the macroscopic crack branching” [45]. In order to proof this assumption for the investigated 17-4PH steel, the sizes of the cracks determined in Figs. 4.17 to 4.20 can be expressed in terms of \sqrt{area} . To measure the projected area of mode II/III crack onto the plane perpendicular to the maximal principal stress, $\sqrt{area_p}$, the crack length must be shortened by a factor of $\sqrt{2}$ while the depth is unaffected. Fig. 4.21 to 4.24 illustrates the projected area of the non-propagating cracks A to D from which the effective value of $\sqrt{area_p}$ can be estimated by the smooth, enclosing contour lines (marked with dashed line).

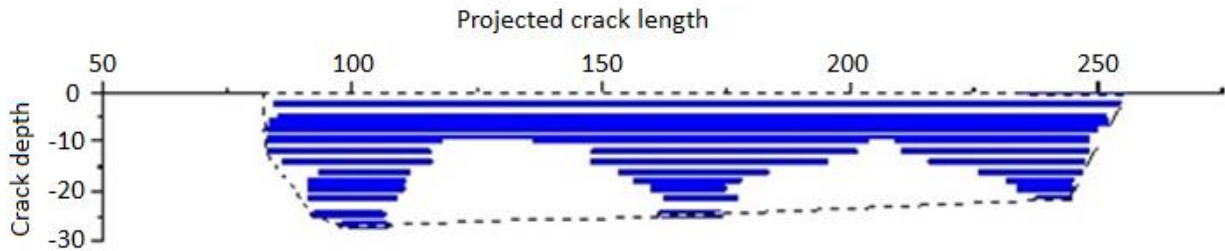


Fig. 4. 21: Size of crack A, $\sqrt{area_p} = 64 \mu\text{m}$.

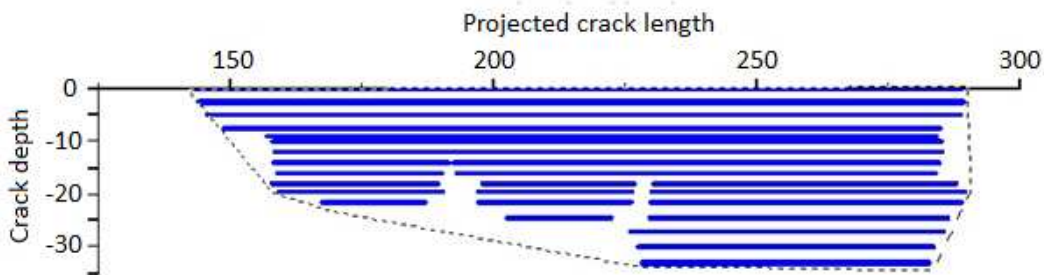


Fig. 4. 22: Size of crack B, $\sqrt{area_p} = 65 \mu\text{m}$.

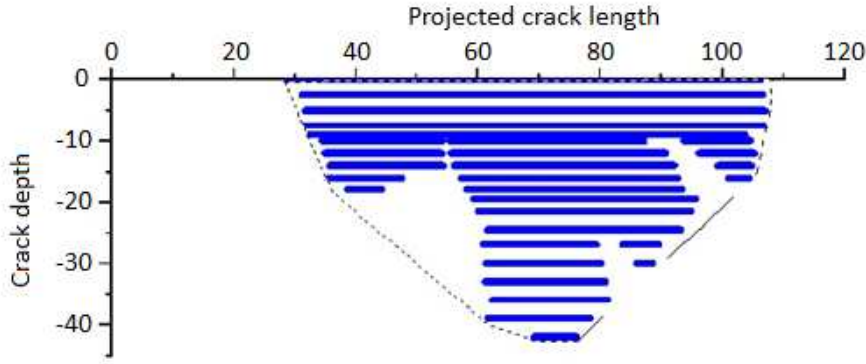


Fig. 4. 23: Size of crack C, $\sqrt{area_p} = 48 \mu\text{m}$.

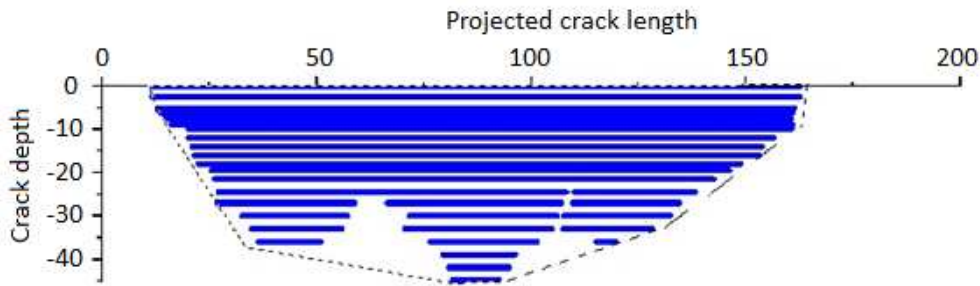


Fig. 4. 24: Size of crack D, $\sqrt{area_p} = 71 \mu\text{m}$.

In order to calculate the Mode I stress intensity factor range of the non-propagating cracks A-D, Eq. (2-11) can be adjusted to:

$$\Delta K_I = 0.65 \cdot (2\tau_w) \cdot \sqrt{\pi \sqrt{area_p}} \quad (4-2)$$

Fig. 4.25 illustrates the comparison between experiment data (Eq. 4.2) and the threshold stress intensity factor range (solid line), which can be calculated as:

$$\Delta K_{th} = 3.3 * 10^{-3} (HV + 120) (\sqrt{area_p})^{1/3} \quad (4-3)$$

It can be seen that the stress intensity of the non-propagating cracks is just below the prediction according to Eq. 4.2. This proves also for the investigated 17-4PH steel that the torsional fatigue limit is determined by the macroscopic propagation of a Mode I crack. It should be noted that the threshold for the Mode I stress intensity factor range for torsional loading is usually by a factor of 0.85 lower compared the threshold for uniaxial loading due to the effect of biaxial stress, see Ref. [46]. However, it could be shown in [39] that the effect of biaxial stress can be neglected in the investigated 17-4PH steel.

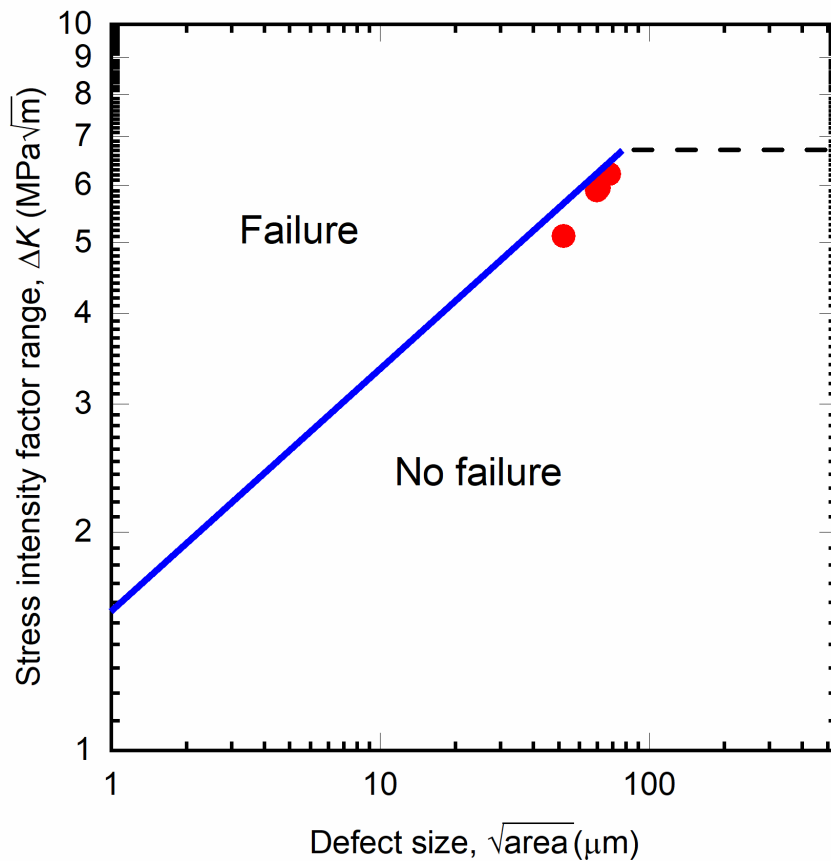


Fig. 4. 25: comparison of experiment data with threshold stress intensity factor prediction line.

4-3 Influences of small defects

According to the occurrence of local stress concentrations, the risk of failure should rise in metallic materials with small surface defects such as scratches, flaws, punch marks and environmentally-induced surface flaws (e.g., corrosion pits) [42]. To investigate the detrimental influence of small defects on 17-4PH stainless steel and its defect tolerance, as described in 3-2, one, two and three artificial holes in different orientations were drilled in the gauge sections of several specimens (see Table 4-1 and Fig. 4-26).

Table 4. 1: properties of different holes.

| Defect type | Characteristic length (μm) | \sqrt{area} (μm) | τ_a (MPa) | <i>N</i> | Failure site |
|-------------------|----------------------------|--------------------|----------------|----------|----------------------|
| 1-hole | 50 | 34 | 360 | 1,13E+07 | Failure from surface |
| | 50 | 34 | 400 | 2,20E+06 | Failure from surface |
| | 50 | 34 | 420 | 3,35E+06 | Failure from surface |
| | 100 | 70 | 330 | 1,41E+08 | Failure from surface |
| | 100 | 70 | 350 | 1,00E+09 | Runout |
| | 100 | 70 | 320 | 1,02E+09 | Runout |
| 2-hole 0° | 50 | 78 | 320 | 4,71E+07 | Failure from holes |
| | 50 | 78 | 310 | 1,02E+09 | Runout |
| | 50 | 78 | 320 | 2,29E+06 | Failure from holes |
| 2-hole 45° | 100 | 161 | 250 | 2,08E+09 | Runout |
| | 100 | 161 | 275 | 2,86E+06 | Failure from holes |
| | 100 | 161 | 260 | 3,33E+06 | Failure from holes |
| 3-hole 0° | 50 | 110 | 290 | 1,02E+09 | Runout |
| | 50 | 110 | 310 | 1,04E+09 | Runout |
| | 50 | 110 | 320 | 3,76E+09 | Runout |
| | 100 | 206 | 230 | 1,59E+09 | Runout |
| | 100 | 206 | 250 | 6,46E+06 | Failure from holes |

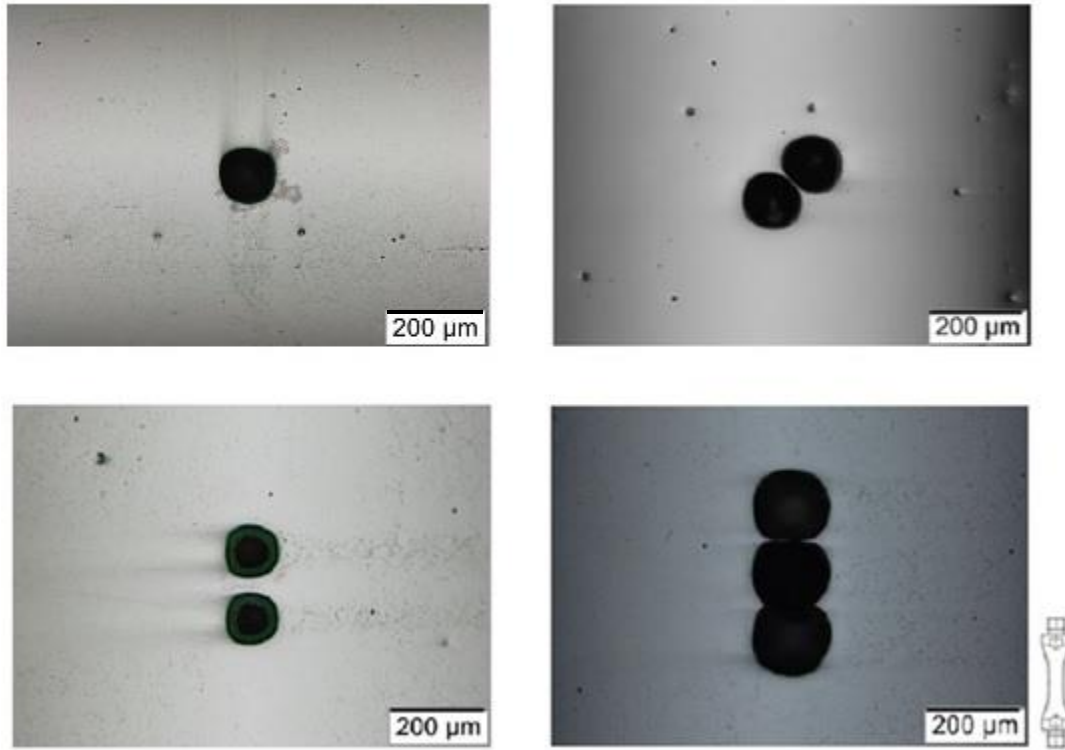


Fig. 4. 26: one, two and three artificial holed in different orientations.

Concerning the specimens with one hole with diameters of 50 μm and 100 μm ($\sqrt{\text{area}} = 34 \mu\text{m}$ and 70 μm), all failures originated from the smooth part of the specimen rather than the hole. It is obvious that this defect had no influence on the fatigue limit. As shown in Fig. 4.27a, the site of crack initiation is not the drilled hole. As shown in Fig. 4.27b, a small crack was nucleated at the hole, but this crack was not detrimental. Another specimen with one drilled hole is illustrated in Fig. 4.28. Fig. 4.28a illustrates the site of cracks on the surface of specimen. The cracks nucleated from smooth site of specimen far from the drilled hole. As shown the drilled hole in Fig. 4.28b, there are again some cracks visible that nucleated at the hole. It cannot be concluded that these short cracks near the hole are non-propagating cracks. Some of the cracks are relatively long and these cracks might have led to failure if the specimen were loaded with higher amplitude.

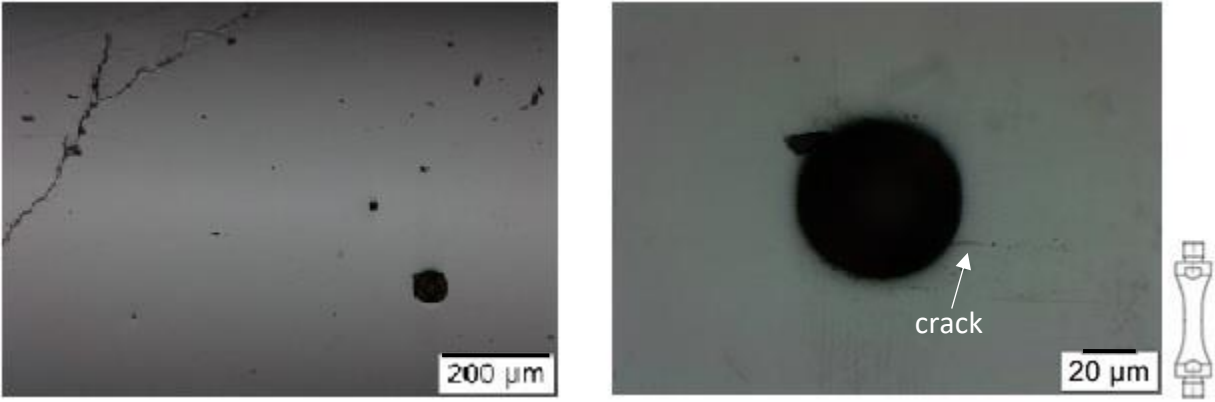


Fig. 4. 27 Fatigue crack growth from smooth part rather than the drilled hole, $R = -1, \tau_a = 360$ and $N_f = 1.13 \times 10^7$
(a) 10x magnification, (b) 50x magnification.

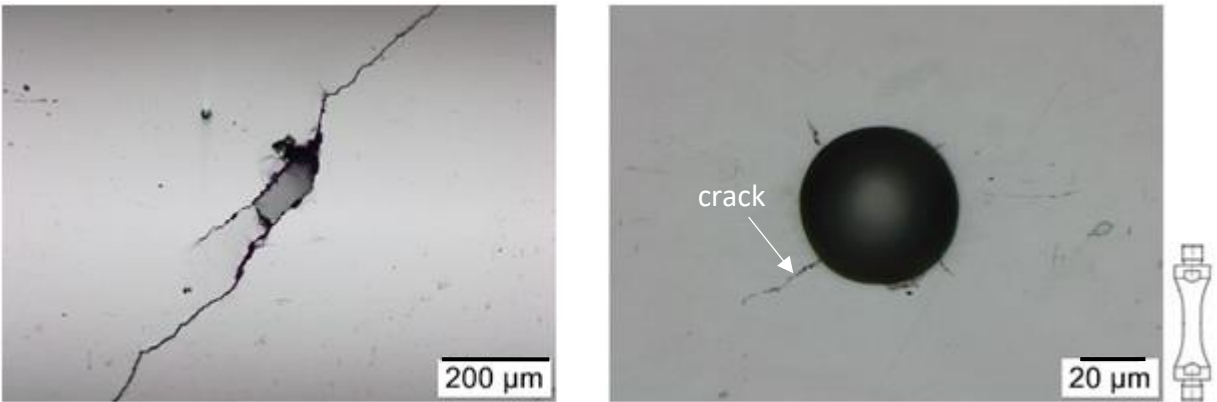


Fig. 4. 28: Fatigue crack growth from smooth part rather than the drilled hole, $R = -1, \tau_a = 420$ and $N_f = 2.2 \times 10^6$
(a) 10x magnification, (b) 50x magnification.

On the other hand, in the specimens with two or three drilled holes, failures clearly initiated from the holes, as can be seen in Fig. 4.29. These cracks already initiated and grew perpendicular to the major principal stress direction (i.e. 45 degrees to the specimen axis).

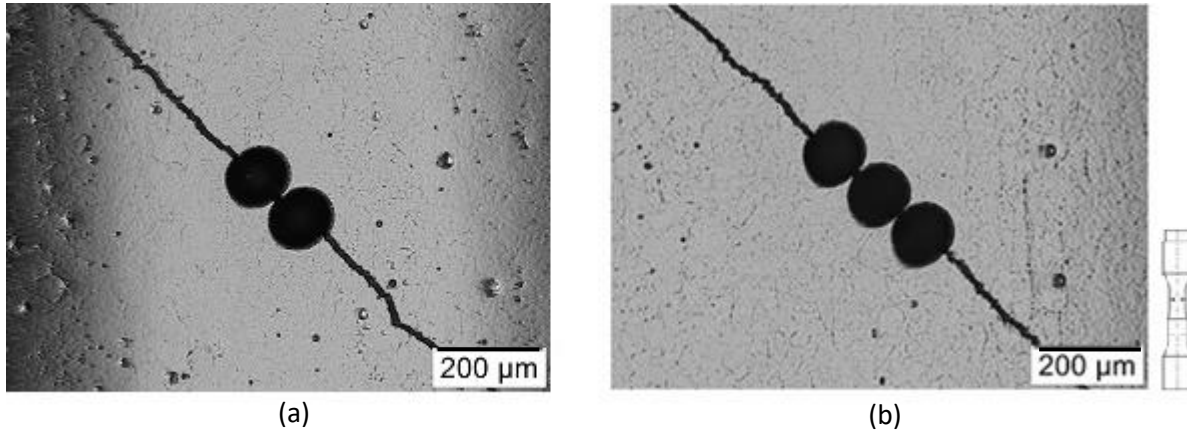


Fig. 4. 29: Fatigue crack growth under torsional loading from (a) two-hole defect, $\tau_a = 260$ and $N_f = 3.3 * 10^6$ and (b) three-hole defect, $\tau_a = 220$ and $N_f = 1.2 * 10^6$ [39].

According to the investigations by Schönbauer et al. on 17-4PH stainless steel, the Mode I threshold stress intensity factor range of a long cracks, $\Delta K_{th,lc}$, is as follows [34]:

$$\Delta K_{th,lc} = 6.7 \text{ MPa}\sqrt{\text{m}} \text{ at } R = -1.$$

The transition size between small and long cracks can be calculated with Eq. 2-13 as $\sqrt{area}_{trans} = 80 \mu\text{m}$. This means that Equation 4.3 does not serve to predict the fatigue limit in the presence of crack or defects larger than $\sqrt{area_p} > 80 \mu\text{m}$, rather the constant value of $\Delta K_{th,lc} = 6.7 \text{ MPa}\sqrt{\text{m}}$ must be applied.

Fig. 4-24 illustrates the relation between torsional fatigue limit, τ_w , and defect size, \sqrt{area} , where the predicted fatigue limit according to Eq. 2.17 and $\Delta K_{th,lc}$ are given as straight blue line. As can be seen, $\Delta K_{th,lc}$ serves well to predict the fatigue strength in the presence of 2- and 3-hole defect. However, the 1-hole defects with sizes in the range of the validity of Eq. 4.3 exhibit lower fatigue strength than predicted. As mentioned above, these 1-hole defects were non-detrimental. The reason for this can be easily explained by the fact that the fatigue limit of smooth specimen is already active, as indicated by the straight, red, dashed-dotted line in Fig. 4.30.

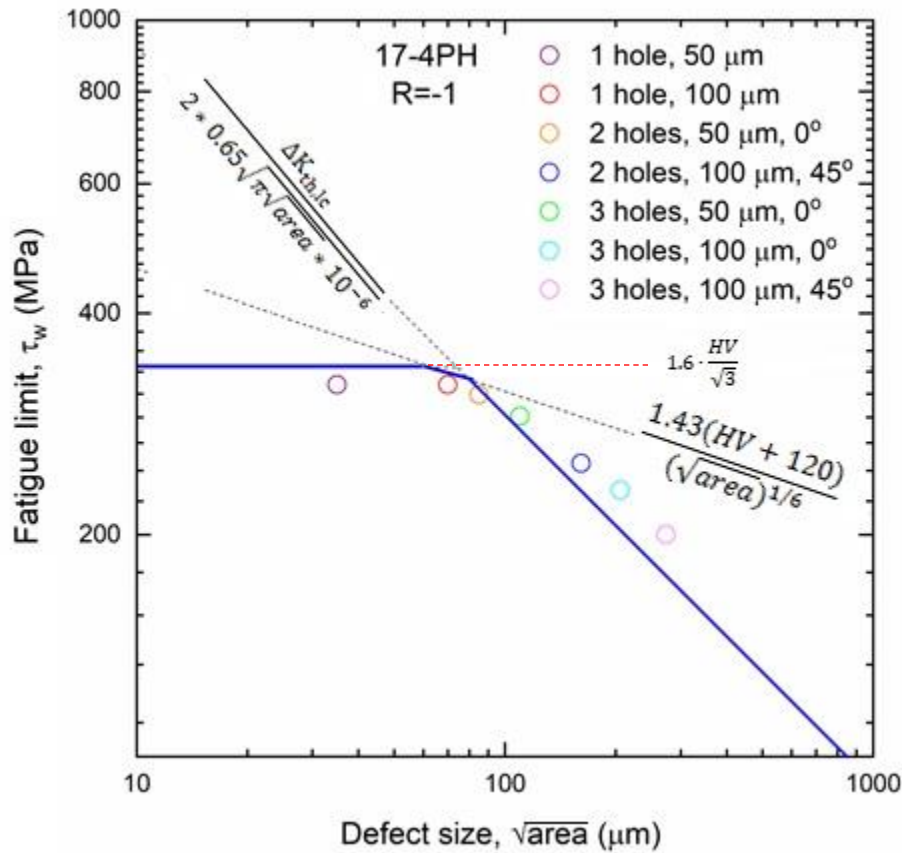


Fig. 4. 30: Relationship between τ_w and \sqrt{area} . Specimens with 1-hole defect failed from the martensitic matrix. All other defects were detrimental. Only runout specimens are given.

4-4 Influence of stress ratio

Torsion fatigue test were performed at two different stress ratios (-1 and 0.05) with smooth specimens and at three different stress ratios (-1, 0.05 and 0.4) with specimens containing 2-hole defects aligned by 45° to the specimen axis with hole-diameters of 100 μm . The *S-N* diagram for smooth specimens and specimens with two-hole defect under torsion loading at different *R*-ratios is illustrated in Fig. 4.31 and Fig. 4.32, respectively. It is obvious that the fatigue limit has been decreased by increasing the *R*-ratio.

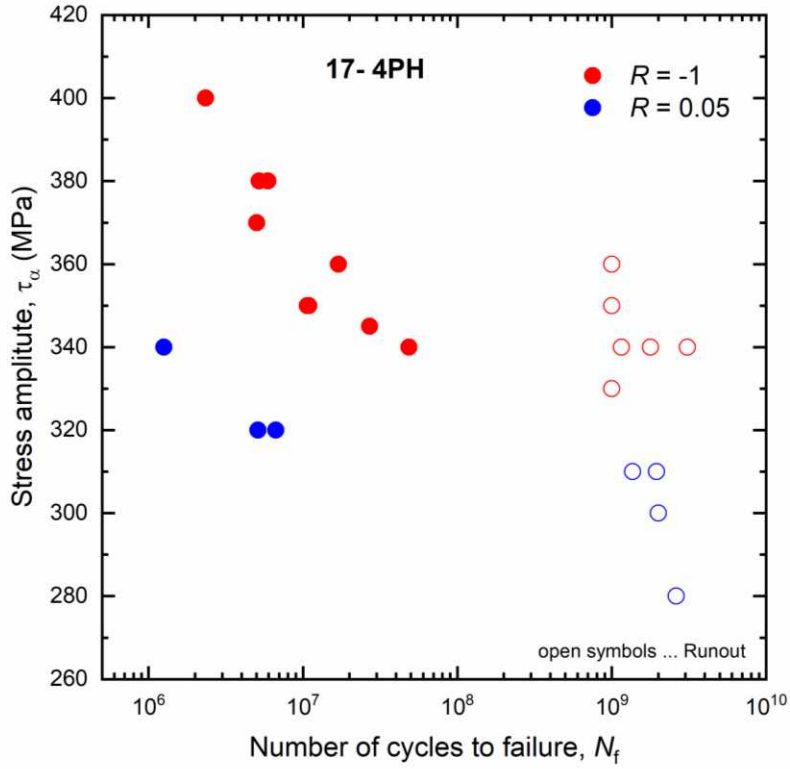


Fig. 4. 31: S-N diagram for smooth specimens under torsion loading at R-ratio of -1 and 0.05.

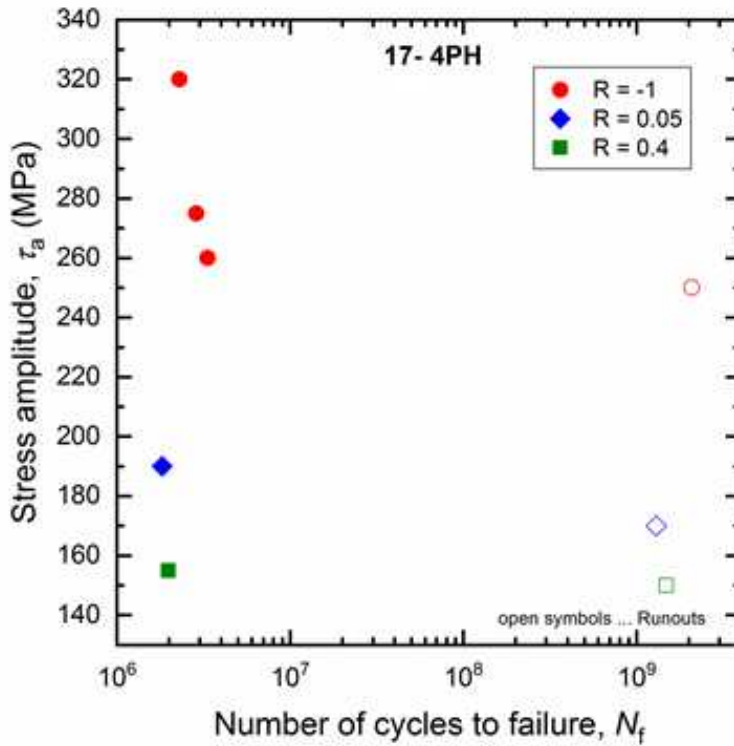


Fig. 4. 32: S-N diagram for two-hole ($100 \mu\text{m}$ diameter and orientation of 45°) defect specimens under torsion loading at R-ratios of -1, 0.05 and 0.4.

To take the R -ratio dependency into account, the \sqrt{area} mode I presented by Murakami can be modified by a correction factor of $\left(\frac{1-R}{2}\right)^\alpha$, so the Eqs. 2-10 and 2-17 can be rewritten as follows:

$$\Delta K_{th} = 3.3 * 10^{-3} (HV + 120) (\sqrt{area})^{\frac{1}{3}} \cdot \left(\frac{1-R}{2}\right)^\alpha \quad (4-4)$$

$$\tau_w = \frac{1.43 (HV + 120)}{(\sqrt{area})^{1/6}} \cdot \left(\frac{1-R}{2}\right)^\alpha \quad (4-5)$$

To estimate the exponent α , Murakami suggested the following equation [23]:

$$\alpha = 0,226 + HV \times 10^{-4} \quad (4-6)$$

However, it has been demonstrated that Eq. (4-6) cannot be applied to the investigated steel 17-4PH [15,16]. Also, the defect size used for investigating the R -ratio dependency is not in the range of small defects, i.e. $\sqrt{area} > \sqrt{area}_{trans}$. Therefore, Eq. 2-18 must be applied. As shown by Schönbauer et al. [16], Eq. 2-18 can be also modified for application at different R -ratios:

$$\tau_w = 434 * \frac{\Delta K_{th,lc}(R = -1)}{(\sqrt{area})^{1/2}} \cdot \left(\frac{1-R}{2}\right)^\alpha \quad (4-7)$$

where $\Delta K_{th,lc}(R = -1) = 6.7 \text{ MPa}\sqrt{m}$ at $R = -1$ according to Schönbauer et al. [34].

To determine the value of α , as shown in Fig. 4.33, $\tau_w \cdot (\sqrt{area})^{\frac{1}{2}} / (434 * \Delta K_{th,lc})$ has been plotted as a function of $(1 - R)/2$ in a double-logarithmic diagram for specimens with different R -ratios. Solid and open symbols mark failed and runout specimens, respectively. A power regression line was drawn through the runout specimens. The slope of this line indicates that $\alpha = 0.433$. The coefficient of determination, $r^2=0.98$, proves that the data is close to regression line.

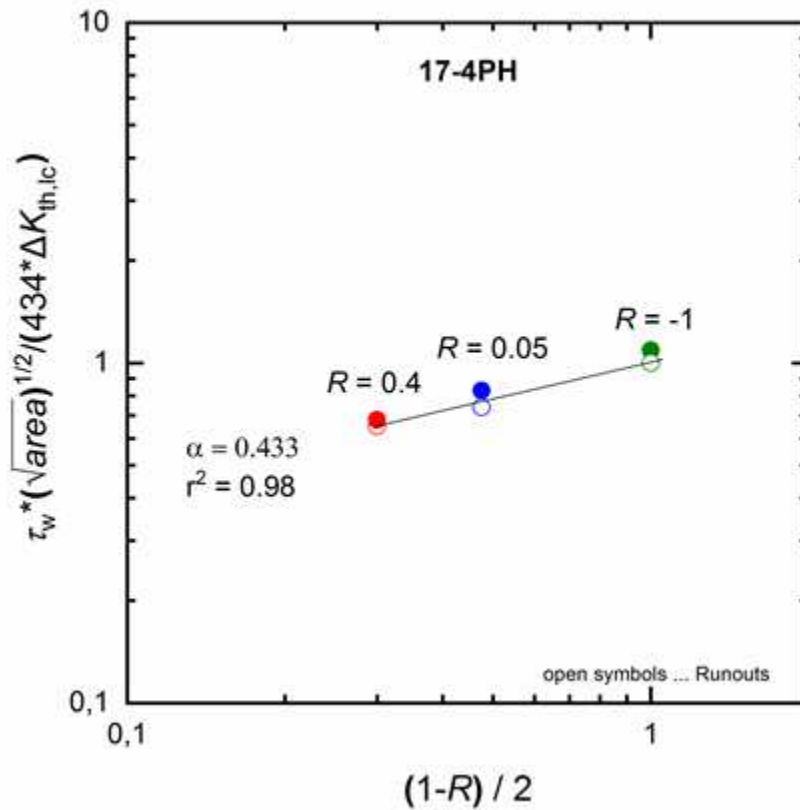


Fig. 4. 33: influence of stress ratio, R , on the fatigue strength.

The determined value of α is consistent with what has been found in a previous study by Schönbauer et al. [16] for the same steel under uniaxial loading at different stress ratios. A value of $\alpha = 0.434$ was determined for uniaxial loading condition. The $\alpha = 0.433$ can be used in the Eqs. 4-5 and 4-7 for different R -ratio. Fig. 4.34 illustrates the relation between stress amplitude and defect size at an R -ratio of 0.05 for both torsional and uniaxial loading (the data of uniaxial loading with different defect types are taken from [16]). It can be noted that the experimentally determined torsional fatigue limit is in good accordance with the predicted fatigue limit and also with the test results under uniaxial loading.

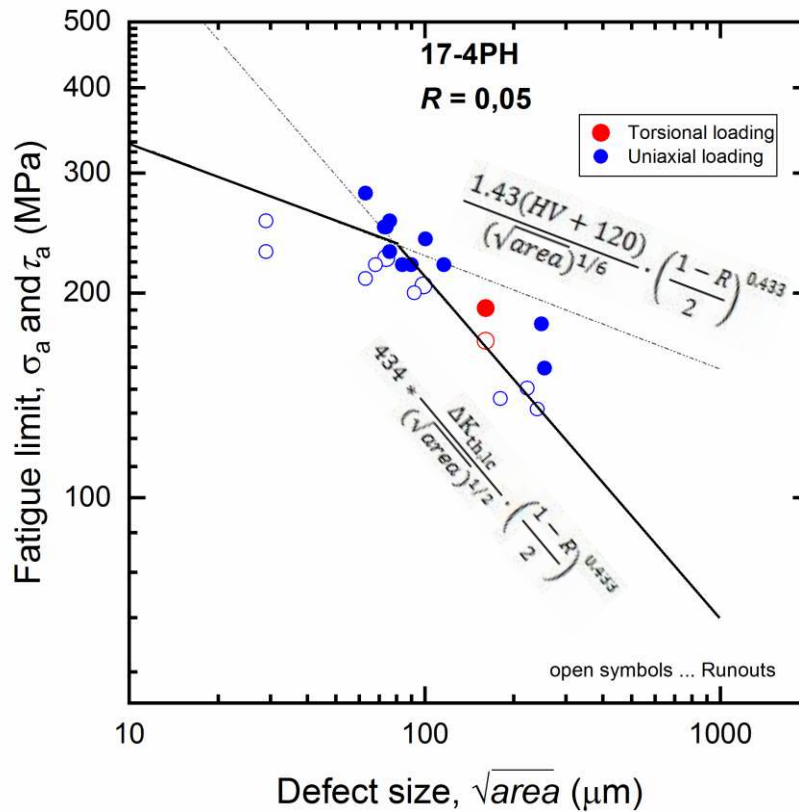


Fig. 4. 34: Stress amplitude, σ_a and τ_a , vs. defect size, \sqrt{area} , at $R = 0.05$. (Uniaxial test results from Ref. [17])

The effect of stress ratio on the fatigue strength can also be illustrated by using a Haigh diagram. The Haigh diagram is drawn by plotting stress amplitude (τ_a, σ_a) on the Y axis and mean stress (τ_m, σ_m) on the X axis (see Fig. 4.35). The mean stress sensitivity (M_σ, M_τ) is defined as:

$$\begin{aligned} \sigma_a &= \sigma_w - M_\sigma \cdot \sigma_m \\ \tau_a &= \tau_w - M_\tau \cdot \tau_m \end{aligned} \quad (4-8)$$

The Haigh diagram of three groups of data including smooth specimens under uniaxial loading [40], smooth specimens under torsion loading and 2-hole specimens under torsion loading is plotted in Fig. 4.35.

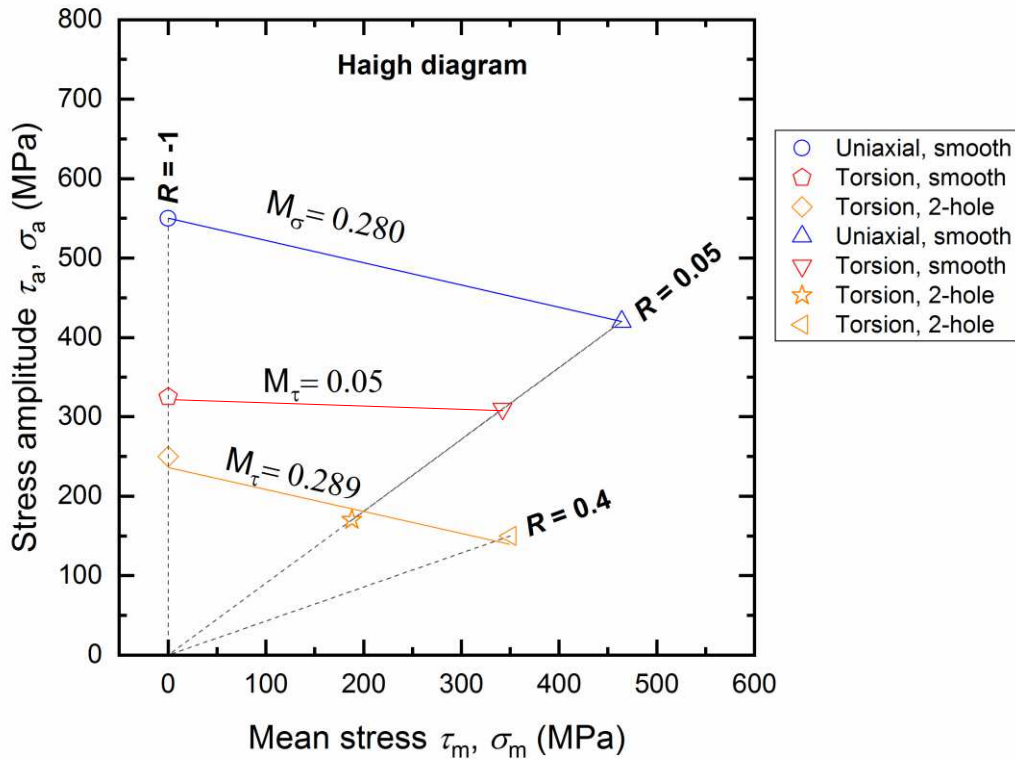


Fig. 4. 35: Haigh diagram of three groups of data including smooth specimens under uniaxial loading, smooth specimens under torsion loading and 2-hole specimens under torsion loading.

According to Fig. 4.35, for smooth specimens under torsion loading (red symbols and line), the mean stress sensitivity is very low, $M_\tau(\text{smooth}) = 0.050$. In contrast, for smooth specimens under uniaxial loading (blue symbols and line) and defect containing specimens under torsional loading (orange symbols and line), the mean stress sensitivity is significantly higher, $M_\sigma(\text{smooth}) = 0.280$ and $M_\tau(\text{2-hole}) = 0.289$, respectively, and the value of M is similar for both. It has to be noted that both smooth specimens under uniaxial loading and 1-hole containing specimens under torsional loading exhibit a similar failure mechanism. In both cases, fatigue cracks initiate at defects (non-metallic inclusions or drilled holes) and these cracks propagate under Mode I. In smooth specimens under torsional loading, in contrast, fatigue cracks initiate in δ -ferrite grains or in the martensitic matrix and crack propagation is initially under Mode II/III. This might be the reason for the different stress ratio dependency.

Chapter 5

Conclusions

In this study, the influence of cyclic frequency and stress ratio on the fatigue properties of precipitation hardened chromium-nickel-copper stainless steel 17-4PH were investigated. Fatigue tests were performed using ultrasonic fatigue testing, and the results were compared with torsional tests that were conducted using conventional servohydraulic testing. Furthermore, to investigate the influence of small defects, various types of holes were drilled in the gauge sections of specimens.

The following results were concluded:

- 1- The different shape of specimens has no significant influence on the torsional fatigue properties.
- 2- The smooth torsional fatigue strength, τ_{w0} , correlates closely to the von Mises criterion, i.e. $\tau_{w0} = \frac{\sigma_{w0}}{\sqrt{3}}$.
- 3- The fatigue strength of specimens tested using ultrasonic fatigue technique was slightly higher compared to low frequency tests and the number of cycles to failure was increased at 20 kHz.
- 4- The 17-4PH stainless steel contains some delta ferrite grains which are elongated in rolling direction of the material.

Performing the fatigue experiment under lower frequency (25 Hz) with conventional servohydraulic test equipment, the deleterious effect of delta ferrite grains on the torsional fatigue strength could be shown. In contrast, failure occurred solely from the matrix (i.e. not from delta ferrite grains) if tests were performed at 20 kHz.

- 5- The shape of non-propagating cracks emanating from delta ferrite grains and from the matrix was determined by successive grinding of specimens. It was found that cracks that

initiated from the delta ferrite grains propagate out of the delta ferrite grains in some places. But, the depths of cracks are in correspondence with the depths of delta ferrite grains. Cracks that initiated from the matrix are rather semi-circularly shaped.

- 6- Concerning the specimens containing one drilled hole, all failures originated from the smooth part of specimens rather than the hole since the size of defects were too small. The torsional fatigue strength of specimens with a defect size smaller than $80\ \mu\text{m}$ can be estimated by the \sqrt{area} parameter model. However, the detrimental size of defects that decrease the fatigue strength is in the same size range which means that the fatigue limit of smooth specimens can be used.
- 7- The \sqrt{area} parameter model is not applicable for defects with sizes larger than $80\ \mu\text{m}$ for the investigated 17-4PH steel. In this case, the threshold stress intensity factor for long Mode I cracks can be used since cracks already initiate under approximately 45° to the specimen axis.
- 8- The torsional fatigue strength with superimposed mean shear loads, i.e. at different R -ratios, was experimentally determined. The mean stress sensitivity M for smooth specimens under torsional loading was found to be very low ($M_\tau = 0.050$). In contrast, the mean stress sensitivity in the presence of detrimental defects is much higher ($M_\tau = 0.289$) and comparable to that under uniaxial loading ($M_\sigma = 0.280$).
- 9- The influence of R -ratio was considered by a correction factor of $(\frac{1-R}{2})^\alpha$. In the presence of detrimental defects that led to Mode I crack initiation, the value of $\alpha = 0.433$ was determined. This value is consistent with what has been found in a previous study for uniaxial loading.

Bibliography

- [1] J. Ratner, B.; Hoffman, A.; Schoen, F.; Lemons, “*Biomaterials Science; An Introduction to Materials in Medicine*,” Academic Press, 2004.
- [2] G. Verma, A. Zarough, and K. Suraliwala, “*Surgical difficulties for Total Knee Replacement in Stickler syndrome: A case report*,” vol. 1. 2008.
- [3] “<https://orthoinfo.aaos.org/en/treatment/total-hip-replacement/>,” [Accessed: 01- Oct- 2019].
- [4] “www.ecnmag.com/product-announcement/2017/05/medtronic-announces-fda-clearance-product-launch-resolute-onyx-drug-eluting-stent,” [Accessed: 01- Oct- 2019].
- [5] “<https://www.klsmartin.com/en/products/implants-hand/>,” [Accessed: 01- Oct- 2019].
- [6] K. S. Katti, “Biomaterials in total joint replacement,” *Colloids Surfaces B Biointerfaces*, vol. 39, no. 3, pp. 133–142, 2004.
- [7] S.-H. Lee, N. Nomura, and A. Chiba, “Significant Improvement in Mechanical Properties of Biomedical Co-Cr-Mo Alloys with Combination of N Addition and Cr-Enrichment,” *Mater Trans*, vol. 49, no. 2, pp. 260–264, 2008.
- [8] A. Carrado, H. Pelletier, and T. Rol, “Nanocrystalline Thin Ceramic Films Synthesised by Pulsed Laser Deposition and Magnetron Sputtering on Metal Substrates for Medical Applications,” in *Biomedical Engineering - From Theory to Applications*, 2011, pp. 411–430.
- [9] J. F. Dyet, W. G. Watts, D. F. Ettles, and A. A. Nicholson, “Mechanical properties of metallic stents: How do these properties influence the choice of stent for specific lesions?,” *Cardiovasc Intervent Radiol*, vol. 23, no. 1, pp. 47–54, 2000.
- [10] I. Mutlu and E. Oktay, “Biocompatibility of 17-4 PH stainless steel foam for implant applications,” *Biomed Mater Eng*, vol. 21, no. 4, pp. 223–233, 2011.
- [11] I. Mutlu and E. Oktay, “Characterization of 17-4 PH stainless steel foam for biomedical applications in simulated body fluid and artificial saliva environments,” *Mater Sci Eng C*, vol. 33, no. 3, pp. 1125–1131, 2013.
- [12] P.E. Schweitzer, A. Philip, “Metallic materials: physical, mechanical, and corrosion properties,” Vol. 19. CRC press, 2003.
- [13] R. L. Liu and M. F. Yan, “The microstructure and properties of 17-4PH martensitic precipitation hardening stainless steel modified by plasma nitrocarburizing,” *Surf Coatings Technol*, vol. 204, no. 14, pp. 2251–2256, 2010.
- [14] H. Mayer, “Recent developments in ultrasonic fatigue,” *Fatigue and Fracture of Engineering*

Materials and Structures," vol. 39, no. 1. pp. 3–29, 2016.

- [15] B. M. Schönbauer, K. Yanase, and M. Endo, "VHCF properties and fatigue limit prediction of precipitation hardened 17-4PH stainless steel," *Int J Fatigue*, vol. 88, pp. 205–216, 2016.
- [16] B. M. Schönbauer, K. Yanase, and M. Endo, "The influence of various types of small defects on the fatigue limit of precipitation-hardened 17-4PH stainless steel," *Theor Appl Fract Mech*, vol. 87, pp. 35–49, 2017.
- [17] K. Yanase, B. M. Schönbauer, and M. Endo, "High cycle torsional fatigue properties of 17-4PH stainless steel," *Frat ed Integrita Strutt*, vol. 10, no. 37, pp. 101–107, 2016.
- [18] Y. Murakami and M. Endo, "Effects of hardness and crack geometry on .DELTA.Kth of small cracks," vol. 35. 1986.
- [19] W. Schütz, "A history of fatigue," *Engineering Fracture Mechanics*, vol. 54, no. 2. pp. 263–300, 1996.
- [20] J. Schijve, "Fatigue of structures and materials," Springer, Berlin Heidelberg, 2009.
- [21] R. M. N. Pelloux, "Mechanisms of formation of ductile striations," *ASM Trans Q*, vol. 1, p. 62, 1969.
- [22] R. E. Peterson, "Stress concentration factors: chart and relations useful in making strength calculations for machine parts and structural element," John Wiley and Sons, 1974.
- [23] Y. Murakami, "Metal Fatigue- Effects of Small Defects and Nonmetallic Inclusions," Elsevier Ltd, 2002.
- [24] G. R. Irwin, "Analysis of Stresses and Strains Near the End of a Crack Traversing a Plate," *Journal of Applied Mechanics*, vol. 24, no. September. pp. 361–364, 1957.
- [25] A. T. Zehnder, "Fracture Mechanics," *Fract Mech*, vol. 62, no. 1, p. 226, 2012.
- [26] F. C. Campbell, "Fatigue and fracture, Understanding the basics," vol. 1. ASM International, 2012.
- [27] P. Paris and F. Erdogan, "A Critical Analysis of Crack Propagation Laws," *J Basic Eng*, vol. 85, no. 4, p. 528, 1963.
- [28] S. Suresh and R. O. Ritchie, "Propagation of short fatigue cracks," *Int Met Rev*, vol. 29, no. 1, pp. 445–475, 1984.
- [29] S. Pearson, "Initiation of fatigue cracks in commercial aluminium alloys and the subsequent propagation of very short cracks," *Eng Fract Mech*, vol. 7, no. 2, pp. 235–247, 1975.
- [30] H. Kitagawa and S. Takahashi, "Applicability of fracture mechanics to very small cracks or the crack in the early stage," 1976, pp. 627–631.
- [31] R.A Smith, "on the short crack limitatins of fracture mechanics," *Int J Fract*, vol. 13, no. 5, pp. 717–720, 1977.
- [32] Y. Murakami and T. Endo, "Effects of small defects on fatigue strength of metals," *Int J Fatigue*, vol. 2, no. 1, pp. 23–30, 1980.
- [33] M. Chapetti, "A simple model to predict the very high cycle fatigue resistance of steels," vol. 33. 2011.

- [34] B. M. Schönbauer *et al.*, “The influence of corrosion pits on the fatigue life of 17-4PH steam turbine blade steel,” *Eng Fract Mech*, vol. 147, pp. 158–175, 2015.
- [35] M. Yukitaka and E. Masahiro, “Quantitative evaluation of fatigue strength of metals containing various small defects or cracks,” *Eng Fract Mech*, vol. 17, no. 1, pp. 1–15, 1983.
- [36] M. Endo, “The multiaxial fatigue strength of specimens containing small defects,” *Eur Struct Integr Soc*, vol. 31, no. C, pp. 243–264, 2003.
- [37] Y. Murakami, S. Kodama, and S. Konuma, “Quantitative evaluation of effects of non-metallic inclusions on fatigue strength of high strength steels. I: Basic fatigue mechanism and evaluation of correlation between the fatigue fracture stress and the size and location of non-metallic inclusions,” *Int J Fatigue*, vol. 11, no. 5, pp. 291–298, 1989.
- [38] D. W. Hetzner, “Etching stainless steels for delta ferrite,” *Adv Mater Process*, vol. 165, no. 2, pp. 33–34, 2007.
- [39] B. M. Schönbauer, K. Yanase, and M. Endo, “Influences of small defects on torsional fatigue limit of 17-4PH stainless steel,” *Int J Fatigue*, vol. 100, pp. 540–548, 2017.
- [40] H. Mayer, “Ultrasonic torsion and tension-compression fatigue testing: Measuring principles and investigations on 2024-T351 aluminium alloy,” *Int J Fatigue*, vol. 28, no. 11, pp. 1446–1455, 2006.
- [41] B. M. Schönbauer, H. Mayer, K. Yanase, and M. Endo, “Torsional fatigue properties of 17-4PH stainless steel in the VHCF regime,” in *Proceedings of Seventh International Conference of Very High Cycle Fatigue*, 2017, pp. 130–135.
- [42] B. M. Schönbauer, H. Mayer, K. Yanase, and M. Endo, “Influence of small defects on the uniaxial and torsional fatigue strength of 17-4PH stainless steel,” *Procedia Struct Integr*, vol. 7, pp. 492–496, 2017.
- [43] N. Tsutsumi, Y. Murakami, and V. Doquet, “Effect of test frequency on fatigue strength of low carbon steel,” in *Fatigue Engng Mater. Struct.*, 2009, vol. 32, pp. 472–483.
- [44] P. Wang, S. P. Lu, N. M. Xiao, D. Z. Li, and Y. Y. Li, “Effect of delta ferrite on impact properties of low carbon 13Cr-4Ni martensitic stainless steel,” *Mater Sci Eng A*, vol. 527, no. 13–14, pp. 3210–3216, 2010.
- [45] M. Endo and K. Yanase, “Near-threshold propagation behavior of small crack in annealed carbon steels under torsional loading,” in *6th International Conference on Crack Paths (CP 2018)*, 2018, pp. 19–21.
- [46] M. Endo and A. J. McEvily, “The growth of short cracks from defects under multi-axial loading,” in *Fracture of nano and engineering materials and structures*, Springer, 2006, pp. 1219–1220.

List of Figures

| | |
|--|----|
| Fig. 1. 1: Examples of metallic implant: (a) artificial knee [2], (b) artificial hip joint [3], (c) artery stent [4], (d) Orthopedic Implant Plates and Screw [5]. | 3 |
| Fig. 2. 1: Constant amplitude cycle loading with $\sigma_m = 0$, (fully reversed cycling loading). | 8 |
| Fig. 2. 2: Constant amplitude cycle loading with positive mean stress σ_m . | 9 |
| Fig. 2. 3: Typical <i>S-N</i> curve. | 11 |
| Fig. 2. 4: Different period of the fatigue life [21]. | 12 |
| Fig. 2. 5: Schematic fatigue fracture surface. | 12 |
| Fig. 2. 6: Typical form of fatigue striation under SEM [21]. | 13 |
| Fig. 2. 7: Stress concentration at an elliptical hole: $\sigma_{yA} = \left(1 + \frac{2a}{b}\right) \sigma_0$, $\sigma_{xB} = -\sigma_0$ [23]. | 14 |
| Fig. 2. 8: Two dimensional crack of length $2a$ [23]. | 15 |
| Fig. 2. 9: Modes of failure, (a): Mode I (opening mode), (b): Mode II (sliding mode), (c): Mode III (tearing mode) [25]. | 16 |
| Fig. 2. 10: Crack length as a function of cycle [27]. | 16 |
| Fig. 2. 11: Typical fatigue-crack-growth diagram showing three different regimes. | 17 |
| Fig. 2. 12: Schematic crack growth rate behavior of short and long cracks. | 19 |
| Fig. 2. 13: Kitagawa-Takahashi diagram | 20 |
| Fig. 2. 14: Definition of \sqrt{area} [23]. | 21 |
| Fig. 2. 15: Murakami and Endo line prediction. | 23 |

| | |
|--|----|
| Fig. 2. 16: Stress transformation on the specimen surface. | 24 |
| Fig. 3. 1: Martensitic microstructure of 17-4PH [15]. | 27 |
| Fig. 3. 2: Surface of specimen after etching and the orientation of delta ferrite grains. | 28 |
| Fig. 3. 3: (a) Cylindrical and (b) hourglass specimen for torsion fatigue test. | 28 |
| Fig. 3. 4: Geometry of servohydraulic fatigue test specimen [17]. | 29 |
| Fig. 3. 5: Equipment for electropolishing. | 29 |
| Fig. 3. 6: End shape of specimens. | 30 |
| Fig. 3. 7: Micro drill machine. | 30 |
| Fig. 3. 8: Oven and centrifuge pump used for residual stress relieving. | 31 |
| Fig. 3. 9: The orientation of difference holes. | 31 |
| Fig. 3. 10: Dimension of artificial drilled holes in μm | 32 |
| Fig. 3. 11: Mechanical setup and load train for ultrasonic cyclic torsion tests: (1) ultrasonic converter, (2) upper mounting part, (3) and (6) ultrasonic horns, (4) vibration gauge, (5) specimen and (7) rotating disc and lower mounting part [15]. | 33 |
| Fig. 4. 1: $S-N$ diagram of smooth cylindrical specimens under torsional loading at $R=-1$ | 35 |
| Fig. 4. 2: $S-N$ diagram of smooth hourglass specimen under torsional loading at $R=-1$ | 35 |
| Fig. 4. 3: Fatigue cracks growth in smooth specimens under torsional loading at $R=-1$ and (a) $\tau_a = 340, N_f = 4.8 \times 10^7$ (b) $\tau_a = 345, N_f = 2.7 \times 10^7$ | 36 |
| Fig. 4. 4: Comparison of $S-N$ data between smooth cylindrical and hourglass specimen at $R=-1$ | 37 |
| Fig. 4. 5: Relationship between fatigue limit in smooth specimens under uniaxial and torsional loading condition [42]. | 38 |

| | |
|--|----|
| Fig. 4. 6: Crack initiation site under uniaxial loading at (a) surface inclusion and (b) Internal inclusion [33]. | 39 |
| Fig. 4. 7: Crack initiation site under torsional loading [41]. | 39 |
| Fig. 4. 8: Influence of different frequency on fatigue strength of specimens.(Data for servohydraulic testing from Ref.[40]) | 40 |
| Fig. 4. 9: Non-propagating cracks observed after testing at the frequency of 25 Hz for a runout specimen at $R=-1$, $\tau_a = 320$ and $N_f = 6 * 10^6$ | 41 |
| Fig. 4. 10: Surface of specimen after etching and the orientation of delta ferrite grains. | 41 |
| Fig. 4. 11: Crack site in delta ferrite region for specimen under torsional loading at frequency of 25 Hz, $\tau_a = 340$ and $N_f = 9.6 * 10^5$, (a) overview, (b) higher magnification. | 42 |
| Fig. 4. 12: Non propagating crack in the delta ferrite region at frequency of 25 Hz, $R=-1$, $\tau_a = 330$ and $N_f = 2.9 * 10^6$. | 42 |
| Fig. 4. 13: Etched specimen after cyclic loading in ultrasonic test equipment at frequency of 20 kHz, $\tau_a = 345$ MPa and $N_f = 2.7 * 10^7$ | 43 |
| Fig. 4. 14: Non-propagating cracks (A+B) formed at delta ferrite grains elongated in role direction. | 44 |
| Fig. 4. 15: Non-propagating cracks (C+D) formed in the martensitic matrix with orientation perpendicular to specimen axis. | 44 |
| Fig. 4. 16: Indentations close to the crack with Vickers hardness testing machine. | 45 |
| Fig. 4. 17: The form of crack A and the delta ferrite region. | 46 |
| Fig. 4. 18: The form of crack B and the delta ferrite region. | 47 |
| Fig. 4. 19: The form of crack C. | 48 |
| Fig. 4. 20: The form of crack D. | 49 |
| Fig. 4. 21: Size of crack A, $\sqrt{area_p} = 64 \mu m$. | 50 |
| Fig. 4. 22: Size of crack B, $\sqrt{area_p} = 65 \mu m$. | 50 |

Fig. 4. 23: Size of crack C, $\sqrt{area_p} = 48 \mu m$51

Fig. 4. 24: Size of crack D, $\sqrt{area_p} = 71 \mu m$51

Fig. 4. 25: comparison of experiment data with threshold stress intensity factor prediction line. 52

Fig. 4. 26: one, two and three artificial holed in different orientations.....54

Fig. 4. 27 Fatigue crack growth from smooth part rather than the drilled hole, $R = -1, \tau_a = 360$
 and $N_f = 1.13 \times 10^7$ (a) 10x magnification, (b) 50x magnification.55

Fig. 4. 28: Fatigue crack growth from smooth part rather than the drilled hole, $R = -1, \tau_a = 420$
 and $N_f = 2.2 \times 10^6$ (a) 10x magnification, (b) 50x magnification.55

Fig. 4. 29: Fatigue crack growth under torsional loading from (a) two-hole defect,
 $\tau_a = 260$ and $N_f = 3.3 * 10^6$ and (b) three-hole defect, $\tau_a = 220$ and $N_f = 1.2 * 10^6$ [38].....56

Fig. 4. 30: Relationship between τ_w and \sqrt{area} . Specimens with 1-hole defect failed from the
 martensitic matrix. All other defects were detrimental. Only runout specimens are given.57

Fig. 4. 31: S-N diagram for smooth specimens under torsion loading at R-ratio of -1 and 0.05..58

Fig. 4. 32: S-N diagram for two-hole (100 μm diameter and orientation of 45°) defect specimens
 under torsion loading at R-ratios of -1, 0.05 and 0.4.58

Fig. 4. 33: influence of stress ratio, R, on the fatigue strength.....60

Fig. 4. 34: Stress amplitude, σ_a and τ_a vs. defect size, \sqrt{area} , at $R = 0.05$.(Uniaxial test results
 from Ref. [17])61

Fig. 4. 35: Haigh diagram of three groups of data including smooth specimens under uniaxial
 loading, smooth specimens under torsion loading and 2-hole specimens under torsion loading.
62

List of Tables

| | |
|--|-----------|
| <i>Table 1.1: Examples of some biomaterials and their applications (according to [1]).....</i> | <i>2</i> |
| <i>Table 1.4: Implants division and type of metals used (according to [8]).....</i> | <i>4</i> |
| <i>Table 3.1: Chemical composition of the 17-4PH in weight %.....</i> | <i>26</i> |
| <i>Table 3.2: Mechanical properties of the 17-4PH at room temperature.....</i> | <i>27</i> |
| <i>Table 4.1: properties of different holes.....</i> | <i>53</i> |